Sharp Interface CFD Analysis of Noncondensable Gas Effects On 1G and Microgravity Tank Self-Pressurization and Pressure Control

Mohammad Kassemi[1, 2 *] and Sonya Hylton[1, 2]

[1]National Center for Space Exploration (NCSER), Case Western Reserve University and NASA Glenn Research Center, Cleveland, Ohio 44135

[2]NASA Glenn Research Center (GRC), Cleveland, Ohio 44135

ABSTRACT

In future refueling depot and space operations, noncondensable gases (NCG)s may be used as pressurants to extract liquid propellant for tank-to-tank transfer and engine start-up operations. Once it is present in the ullage, the noncondensable gas can affect the interfacial evaporation and condensation processes that control tank self-pressurization and pressure control during subsequent storage. The Zero-Boil-Off-Tank-Noncondensable (ZBOT-NC) Experiment and its associated computational model development effort are carried out to study these phenomena. In this work, we present a Sharp Interface CFD (SI-CFD) model which is applied to the two-phase and two-component simulant fluid system used in the ZBOT-NC Experiment with Perfluoro-n-Pentane (PnP) as the *simulant* low-boiling point phase change fluid, and Xenon as the noncondensable gas. The SI-CFD model solves the continuity, momentum, energy, species, and turbulence equations in the vapor and liquid phases while providing very accurate temperature and species gradient calculations at the interface. In developing this model, particular attention was focused on the precise determination of the molar concentrations of the vapor and the noncondensable gas at the interface in order to correctly predict the vapor "Stefan wind" in the ullage, as well as the extent of the accumulation of the noncondensable gas at the phase front. Detailed microgravity and 1g numerical simulations and analyses are presented to show the characteristics of the noncondensable gas induced transport resistance in the ullage, along with the thermocapillary (Marangoni) convection in the liquid and their impact on the interfacial heat and mass transfer during tank self-pressurization and jet mixing pressure control. The results of these simulations indicate that, in 1g, the presence of the noncondensable gas affects pressure control noticeably but its impact on self-pressurization is minimal. However, in microgravity, the noncondensable gas seems to have a noticeable impact during self-pressurization while its effect on jet mixing pressure control is significant and considerably more pronounced than on earth.

Introduction

Future refueling depot operations in space require the transfer of propellants from the donor tank to the receiver tank under weightlessness conditions. For long duration depot applications, it is advantageous to perform the transfer by pressurizing the donor tank using a gaseous pressurant rather than using a mechanical pump which is more prone to failure. Tank pressurization can be accomplished either autogenously by using a like gas (the vapor of the liquid fuel that is being stored and transferred), or by using a noncondensable pressurant gas such as helium. However, noncondensable gas pressurization seems to be an attractive option since it can be accomplished

faster and with minimal additional hardware. Unfortunately, once the noncondensable gas is present in the ullage, it can interfere with the condensation and evaporation processes at the liquid-vapor interface and may therefore have important consequences for tank self-pressurization and pressure control during subsequent storage periods.

The effects of noncondensable gas on phase change, especially in relation to its impact on the condensation process in two-phase heat exchangers and phase separators, have been the subject of considerable experimental and computational research. However, the same level of scientific and engineering scrutiny has not been focused on the effects of noncondensable gas on the transport and phase change processes that take place in cryogenic propellant tanks on the ground or in microgravity. The Zero-Boil-Off Tank–Noncondensable (ZBOT-NC) microgravity investigation is the first hand-in-hand science experiment and CFD model development effort that is devoted to elucidating the impacts of noncondensable gases on the phase change and transport processes that govern pressurization and pressure control of a volatile fluid in a sealed tank in 1g and microgravity. In this paper, we present a two-phase two-component CFD model that has been developed to capture the effects of noncondensable gas on the interfacial evaporation-condensation and bulk transport processes in the ZBOT-NC experiment. The experiment is anticipated to begin operations on the International Space Station (ISS) in the near future and will collect valuable data for the future validation of this model.

The effects of noncondensable gases on vapor condensation heat and mass transfer have received noticeable attention from the experimental and theoretical/computational heat transfer communities due to their importance in a variety of high efficiency two phase heat transfer equipment such as heat pipes, nuclear reactor towers, refrigeration units, air conditioning radiators and phase separators. Because of this direct terrestrial technological interest, the focus of the research has mostly been on vertical and horizontal flat plates or pipe geometries in water/steam systems with air or other inert gases as the noncondensable component.

Donald Othmer [1] was the first to perform an experimental investigation of steam condensation in the presence of a NCG. In his experiment, he placed a horizontal copper tube, with cooling water flowing through it, in a small boiler. He observed that when the volume fraction of air in the boiler was raised to 0.5%, the surface heat transfer coefficient of the tube fell by 50%. Subsequently, many researchers experimentally studied condensation in the presence of various kinds of noncondensable gases, including air, nitrogen, argon, neon, and hydrogen on vertical and horizontal surfaces under forced or natural/free convection and observed the same inhibitory heat and mass transfer effects [2].

The theoretical treatments of NCG effects have mostly been concerned with film-wise condensation on flat or cylindrical surfaces and can be divided into two groups. The first group, as exemplified by the works of Minkowycz and Sparrow [3] and Sparrow et al. [4], used a boundary layer configuration to describe heat and mass transfer from a mixture of steam and air on a vertical flat isothermal plate. In their comprehensive analytical treatment, they included the effects of free solutal and thermal convection, superheating, mass and thermal diffusion, interfacial kinetic resistance, and variable properties. Their results, which were obtained over a wide range of system parameters, agreed with the previously mentioned experimental findings, and confirmed that for even a small 0.5% bulk mass fraction of air, a 50% reduction in the heat transfer may have to be sustained. It was shown that the reductions of heat and mass transfer were mostly due to the diffusional resistance of the gas-vapor boundary layer, and that the interfacial resistance to heat transfer had a second order effect.

The second group of theoretical studies, initiated by Colburn and Hougen [5], proposed a diffusion layer model, where it is assumed that the NCG accumulation forms a diffusion layer and hinders the transport of vapor to the interface. Kageyama et al [6], Peterson [7], and Revankar and Pollock [8] conducted an in-depth analysis of the problem using this approach. Kageyama and Pollock [8] used a 9-step calculation method to solve for the model parameters and calculate the total and partial condensation heat and mass transfer coefficients. However, due to the difficulty of the analysis and the lack of direct experimental confirmation, the diffusion model has not gained widespread acceptance [2].

Panzarella and Kassemi [9] considered the effect of noncondensable gases in an idealized one-dimensional purely diffusive-advective flow across an infinite layer bounded on the top by an evaporating flat interface and on the bottom by a condensing flat interface. The interfaces were kept at different temperatures, with noncondensable gas in the intervening vapor region; the mass transfer at either interface was represented by the Schrage kinetics equation. The analysis assumed small temperature differences between the evaporating and condensing interfaces and identified three distinct mass-transport regimes depending on the magnitude of the characteristic noncondensable mole ratio, x, relative to the critical characteristic mole ratio, x_c, which is a measure of the importance of diffusive versus kinetic effects. It was found that when $x << x_c$, the system is in a kinetically-limited regime, where the mass flux approaches an upper limit dictated by kinetic effects. When $x_c << x << 1$, the kinetic effects become negligible, and the mass flux is determined by a combination of diffusive and convective contributions, with the diffusive contribution becoming more important as x increases. Finally, when $x >> 1$, the system is in a diffusively-limited regime, where the mass flux approaches another constant value as the system becomes saturated with noncondensable gas. Application of the relationships that were developed as part of this analysis to a particular situation involving the cryogenic storage of liquid hydrogen led to two important conclusions. First, in the absence of a noncondensable gas, the interfacial temperature will be uniform and equal to the saturation temperature. In this case, a significant heat flux is required to produce any appreciable non-uniformity in the interfacial temperature. Second, in the presence of even a minute amount of noncondensable gas, temperature variations can be sustained between different evaporating and condensing sites on the vapor–liquid interface at quite moderate heat fluxes. In this situation, surface-tension variations caused by the resulting interfacial temperature gradients could potentially give rise to thermocapillary (Marangoni) convection.

Straub [10, 11] performed a series of microgravity boiling studies in the BDPU test facility aboard the LMS Space Shuttle mission, in the 1996-1997 time frame. In one of these experiments, nucleate boiling was generated on a 1mm diameter circular heater in a transparent simulant refrigerant fluid (R123). One of their most interesting results was the unexpected observance of Marangoni (thermocapillary) convection that emanated from the bubble like a jet flow and was captured by an interferometric setup in the BDPU facility. This was a non-intuitive outcome, since during boiling, according to equilibrium thermodynamics, the bubble interface is expected to be at a uniform saturation temperature dictated by the uniform bubble vapor pressure. An additionally curious feature of the flow was that the subcooled temperature difference did not seem to be the driver for the Marangoni convection. It was postulated that the flow was driven by the partial pressure variations in the ullage that were caused by the accumulation of noncondensable gases that were dissolved in the fluid.

In a more recent analysis, Balasubramaniam and Rame [12] analyzed the condensation of a quiescent vapor that is in equilibrium with its liquid and is induced by a stagnation point flow in the liquid. Their stagnation flow configuration is applicable to the subcooled jet mixing pressure

control process in a propellant storage tank. Here, the liquid flow brings subcooled liquid from far away to the interface. The ensuing heat transfer causes the vapor to condense. Exploiting a similarity formulation for the liquid and vapor flow fields, and using a perturbation analysis, a solution was provided for a small ratio of the product of viscosity and density of the vapor to that of the liquid. The results of a two-term higher order asymptotic solution confirmed the reduction of the interfacial condensation rate due to the presence of the noncondensable gas in the vapor.

Experimental assessments of the impacts of noncondensable gases on propellant storage tank pressurization and pressure control on the ground have been very limited, while no such experiment seems to have been conducted in microgravity. Theoretical and computational treatments of these phenomena have also been limited, and do not cover geometries and fluid systems which are pertinent to propellant storage tanks. One of the early ground-based investigations of the effects of a noncondensable pressurant on tank pressure control was carried out by Bullard [13] at Lockheed in 1972. This 1g experiment was performed in a 2.8 meter tank and produced more than 1500 hrs of liquid hydrogen (LH2) thermal conditioning test results, with both gaseous helium (GHe) and gaseous hydrogen (GH2) as pressurants. A TVS system which was assisted by a mixing jet was used after the initial pressurization of the tank for pressure control/reduction, and the effects of various parameters such as jet mixing, fill level, and pressurant gas levels and temperatures were investigated. The depressurization data showed substantial reductions in the pressure drop rate for the TVS cooling tests, both with and without mixing, when the tank was pressurized with the noncondensable gaseous He rather than the like H2 vapor. In the TVS-cooling tests which were accompanied by a 0.7 kg/hr jet mixing flow rate, the overall rate of depressurization was around 10 times slower for the case with the GHe noncondensable.

A more recent pressurized tank sloshing experiment performed in 1g by the University of Tokyo and JAXA [14] investigated the depressurization of a pure LN2 system versus a multicomponent system where the tank was pressurized with GHe. The data again indicated a remarkable drop in the depressurization rates when the noncondensable gas was used. Unfortunately, the experiments were performed at the same initial tank total pressure, rather than the same initial tank LN2 vapor partial pressure. Thus, the driving force for the condensation was not the same in the two tests. Nonetheless, the smaller initial vapor pressure in the GHe pressurized case cannot entirely account for the significant drop in the condensation mass transfer that occurred.

In this work, we present a Sharp Interface CFD (SI-CFD) model that is applied to the two-phase simulant fluid system that will be used in the ZBOT-NC pressurization and pressure control experiment, with Perfluoro-n-Pentane (PnP) as the *simulant* low-boiling point phase change fluid, and xenon as the noncondensable gas. The numerical model is developed and implemented into the framework of the ANSYS/Fluent CFD code through in-house customized and coded User-Define Functions (UDF)s. The SI-CFD model solves the continuity, momentum, and energy equations in the vapor and liquid phases, along with the species equation in the ullage domain, while providing very accurate temperature and species gradient calculations at the interface [15]. In the sections that follow, the mathematical formulation of the two-phase two-component pressurization and pressure control model are presented, and the numerical methodology used to perform the simulations are discussed. Next, detailed microgravity and 1g numerical simulations and analyses are presented to show the characteristics of the transport resistance that is created in the ullage and the thermocapillary (Marangoni) convection that is induced in the liquid by the noncondensable gas, along with their impact on the interfacial heat and mass transfer during tank self-pressurization and jet mixing pressure control. The results of these simulations indicate that

the effect of the noncondensable gas on self-pressurization is minimal in 1g, although it's noticeable in microgravity, while its effect on pressure control is noticeable in 1g but significantly more pronounced in microgravity.

Mathematical Formulation

A sketch of the ZBOT-NC experimental tank inside the vacuum jacket is displayed in Fig. 1, and an axisymmetric cross-section of this geometry with the ullage and liquid domains in 1g and microgravity was used to create the computational grids for the simulation studies that are shown in Fig 2. In the Sharp Interface, or SI-CFD, model, the liquid and ullage regions are separated by a sharp, rigid, flat (1g) or curved (μg) boundary that represents the interface. In general, the ullage domain is occupied by a mixture of PnP vapor and noncondensable gaseous xenon that is compressible and follows the ideal gas law. Since xenon has a relatively low solubility in PnP, the interface is assumed to be impermeable to the noncondensable gas. The liquid domain is therefore occupied only by liquid PnP, which is treated as an incompressible fluid. The fluid flow in both domains is considered to be laminar. The governing continuity, Navier stokes, and energy equations are written and solved separately for both the liquid and ullage domains. But the species conservation equation is written only for the ullage and the interface is assumed to be impermeable to the noncondensable gas (xenon). However, the two phases are coupled together through the continuity of velocities, temperature, and mass flow and the balances of shear stress, and energy at the sharp interface.

The set of equations describing fluid flow and conservation of energy and species for the gas mixture in the ullage domain are presented below. The continuity equation is written as:

$$\frac{\partial \rho}{\partial t} + \vec{\nabla} \cdot (\rho \vec{v}) = S_C \tag{1}$$

Where ρ is the fluid density, $\vec{v}$ is the velocity vector, t is time, and S_C is a mass source term.

The momentum equation is given by:

$$\frac{\partial \rho_m \vec{v}_m}{\partial t} + \vec{\nabla} \cdot (\rho_m \vec{v}_m \vec{v}_m) = -\vec{\nabla} P + \mu_m \vec{\nabla} \overline{\overline{\mathrm{T}}}_m + \rho_m \vec{g} + S_M \tag{2}$$

where the fluid shear stress tensor, $\overline{\overline{\mathrm{T}}}$, is defined as:

$$\overline{\overline{\mathrm{T}}}_m = \left(\nabla \vec{v}_m + \nabla \vec{v}_m{}^T\right) - \frac{2}{3}\left(\vec{\nabla} \cdot \vec{v}_m I\right) \tag{3}$$

Here, P is the fluid pressure, μ is the fluid kinematic viscosity, $\vec{g}$ is the gravitational vector, and S_M is a momentum source term. The dissipation term in the momentum equation is neglected.

The conservation of energy equation for the fluid is given by:

$$\frac{\partial \rho_m E_m}{\partial t} + \vec{\nabla} \cdot [\vec{v}_m (\rho_m E_m + P)] = \vec{\nabla} \cdot \left(k_m \vec{\nabla} T_m - \sum_j h_{m,j} \vec{J}_{m,j}\right) + S_E \tag{4}$$

where E is the internal energy, h is the enthalpy, and S_E is an energy source term. The summation term in Eq (4) accounts for the transport of energy by molecular diffusion in the gas mixture. Since the Lewis number ($\frac{k_m}{\rho_m c_{p,m} D_{i,m}}$) for the PnP-xenon mixture is smaller than one, this term's contribution to the energy transfer is quite small.

The conservation of species equation is:

$$\frac{\partial \rho_m Y_v}{\partial t} + \vec{\nabla} \cdot (\rho_m \vec{v}_m Y_v) = -\vec{\nabla} \cdot \vec{J}_v + S_Y \tag{5}$$

In this equation, Y is the species mass fraction, S_E is the species source term, and following Fick's law the mass diffusion flux vector, $\vec{J}$, is defined as:

$$\vec{J}_v = -\rho D_{i,m} \vec{\nabla} Y_v \tag{6}$$

where $D_{i,m}$ is the molecular diffusion coefficient for species *i*. In Eq (6), the effect of thermal or Soret diffusion is neglected. Constant composition-dependent properties based on mixture laws were used in the above equations for the gas mixture except for the density, which is obtained using the ideal gas relationship:

$$\rho_m = \frac{P}{RT_m \sum_j (Y_j / M_{w,j})} \tag{7}$$

Here $M_{w,m} = \sum_j \left(Y_j / M_{w,j}\right)$ is the molecular weight of the mixture, and *R* is the universal gas constant.

The same set of equations can be written for the liquid domain by interchanging the subscript "m" which is used for the gas mixture with a subscript "l" to denote the liquid. Since the liquid is treated as an incompressible fluid, the divergence terms in Eqs. (1) and (2) for continuity and momentum are set to zero, and the density is also assumed to be constant in all of the terms except for the buoyancy term in the momentum equation, where it is represented by the linearized Boussinesq relationship as:

$$\rho_l = \rho_{o,l}[1 - \beta_l (T_l - T_o)] \tag{8}$$

In order to perform a conjugated heat transfer analysis with two way coupling, the following energy equation is used to account for the wall conduction:

$$\rho_w c_w \frac{\partial T_w}{\partial t} = \vec{\nabla} \cdot \left(k_w \vec{\nabla} T_w\right) \tag{9}$$

Equations (1) – (9) represent the complete set of equations for the liquid, the ullage, and the wall domains in the present noncondensable CFD model. However, these three regions are also coupled to each other by the momentum, energy, and species interface conditions and the conjugated heat transfer boundary conditions for the tank wall.

For the momentum equation, the normal and tangential velocities for the liquid and gas mixture are related to each other by the continuity of tangential and normal velocities across the interface. For the normal velocities we have:

$$\rho_l \vec{v}_l \cdot \hat{n} = \rho_m \vec{v}_m \cdot \hat{n} = \vec{J}_{PC} \cdot \hat{n} \tag{10}$$

But since the phase change mass flux is small and the density of the liquid is large, in the present model these equations were approximated by

$$\rho_l \vec{v}_l \cdot \hat{n} = 0 \tag{11a}$$

and

$$\rho_m \vec{v}_m \cdot \hat{n} = \vec{J}_{PC} \cdot \hat{n} \tag{11b}$$

the tangential velocities at the interface are related to each other as:

$$\vec{v}_l \cdot \hat{t} = \vec{v}_m \cdot \hat{t} \tag{12}$$

Balancing the shear stresses at the interface requires that:

$$\left(\mu_l \overline{\overline{\mathrm{T}}}_l - \mu_m \overline{\overline{\mathrm{T}}}_m\right) \cdot \hat{n} \cdot \hat{t} = \vec{\nabla}_S \sigma_l \cdot \hat{t} = \Gamma_T \vec{\nabla}_S T_l \tag{13a}$$

where σ_l is the liquid surface tension, and Γ_T is the temperature coefficient of surface tension that are related to each other by the following linearized equation:

$$\sigma_l = \sigma_{l,o} + \Gamma_T (T_l - T_o) \tag{13b}$$

For the energy equation, the continuity of the liquid, vapor, and interface temperatures that prevails for near equilibrium conditions at the phase front requires that:

$$T_l = T_m = T_I \tag{14}$$

Moreover, the most important equation in two-phase problems that involve interfacial condensation and evaporation is the energy balance at the phase front that relates the interfacial phase change mass flux to the heat fluxes at the gas and liquid sides of the interface:

$$L_{lv}\left(\vec{J}_{PC} \cdot \hat{n}\right) = k_m \vec{\nabla} T \cdot \hat{n} - k_l \vec{\nabla} T \cdot \hat{n} \tag{15}$$

The interfacial phase change mass flux that appears in Eqs. (10), (11b) and (15) can be evaluated from a widely used kinetics phase change mass transfer relationship by Schrage [16] as:

$$\vec{J}_{PC} \cdot \hat{n} = \frac{2\alpha}{2-\alpha}\left(\frac{1}{2\pi r T_I}\right)[P_{sat}(T_I) - P_v] \tag{16}$$

Where α is the kinetics accommodation coefficient, and P_{sat} is the saturation pressure, which in this work is defined by the Clausius Clapeyron equation:

$$\ln\left(\frac{P_{sat}}{P_r}\right) = \frac{L_{lv}}{R}\left(\frac{1}{T_r} - \frac{1}{T_I}\right) \tag{17}$$

The evaporating or condensing phase change mass flux, $\vec{J}_{PC}$, which is the main driver for pressure changes in the sealed tank, can be evaluated following two different methods. In the first method, the interface is assumed to be at the saturation temperature ($T_I = T_{sat}(P_v)$), and the mass flux is then calculated directly from the energy balance in Eq (15). In the second method, which is used in the present paper, Eqs. (14)-(17) can be used to derive a single nonlinear equation for the interface temperature which is solved using a Newton Raphson method. Once the interface temperature is determined, the phase change mass flux can be evaluated from Eq (16). Kassemi and Kartuzova [17] have shown that the T_I that is calculated by the second scheme is equal to T_{sat} for near equilibrium conditions and small mass fluxes for any accommodation coefficient value, but T_I can deviate from T_{sat} when the phase change mass transfer is large and near equilibrium conditions no longer hold.

Finally, there are two boundary conditions for the conjugated heat transfer equation. At the inner tank wall surface, we have:

$$k\left(\vec{\nabla} T \cdot \hat{n}\right) = k_w\left(\vec{\nabla} T_w \cdot \hat{n}\right) \tag{18}$$

and at the outer wall surface we have:

$$-k_w\left(\vec{\nabla} T_w \cdot \hat{n}\right) = -k_{N2}\left(\vec{\nabla} T_{N2} \cdot \hat{n}\right) + q_{RAD}\left(T_{VJ}\right) \tag{19}$$

In Eqs. (18) and (19), k and T refer to either the liquid or the gas mixture, k_{N2} and T_{N2} refer respectively to the conductivity and temperature of the gaseous nitrogen that occupies the annular region between the tank and the vacuum jacket, and q_{RAD} represents the surface-to-surface radiation heat transfer that takes place between the inner surface of the vacuum jacket and the outer surface of the tank wall.

Numerical Implementation

Ansys Fluent Version 23 was used to perform the CFD simulations that solve the continuity, momentum, species, and energy equations for an axisymmetric model. The radiation heat transfer between the tank and VJ walls was modeled using the existing Surface-to-Surface radiation capabilities in Ansys Fluent. Because the interface was assumed to be impermeable to the noncondensable gas, the species equation was only solved for the vapor and xenon gas mixture

in the ullage domain. The jet flow was considered to be laminar. The fluid material properties were constant apart from the density; for the densities of the vapor and noncondensable gas, the ideal gas law was used, while the Boussinesq approximation was used to represent the variation of density with temperature in the buoyancy term for the liquid and for the nitrogen gas that filled the vacuum jacket. The PnP-xenon mixture properties used the ideal gas law for the density, a composition dependent mixing-law for the specific heat, the ideal gas mixing law for the thermal conductivity and viscosity, and a constant value for the diffusivity. The thermophysical properties of the liquid and vapor were obtained from the DIPPR database [18].

The transient simulations were performed using Fluent's Bounded Second Order Implicit scheme. The pressure-velocity coupling was solved using Ansys Fluent's PISO scheme, where the pressure was discretized by the body force weighted approach. A second order upwind scheme was used to discretize the density, momentum, species, and energy equations. The gradients were computed using the Least Squares Cell Based method. The convergence criteria for the momentum and species equations were set to 10^{-5}, while the convergence criterion for the continuity was set to 10^{-4}, and the convergence criterion for the energy was set to 10^{-6}.

Mathematical formulations for the energy and momentum and species balances at the liquid-vapor interface were developed, coded, and implemented into Fluent using User Defined Functions (UDFs). The evaporation and condensation mass transfer rates were also calculated via UDFs using the Schrage relation and applied as volumetric source terms in the vapor region. To implement the momentum balance at the interface, the velocity of the liquid at the interface was imposed on the vapor, and the shear stress from the vapor side together with the Marangoni contribution were imposed on the liquid at the interface via UDFs. Appropriate source/sink terms were also incorporated via dedicated UDFs for mass, species, and energy for the first computational cell in the ullage next to the interface to account for contributions due to phase change mass transfer.

The resulting set of equations was solved using Fluent's Algebraic Multi-Grid (AMG) solver. Fig. 2 shows the unstructured quad meshes that were used for the CFD simulations, where selective grid refinement was applied at the wall and interface boundaries, as well as along the path of the jet for the pressure control simulations. These different optimum mesh sizes were selected based on careful grid convergence studies for both the 1g and microgravity self-pressurization and jet mixing simulations using the tank pressure as the basis for the comparisons.

Results and Discussion

A diagram of the ZBOT-NC tank and its supporting hardware and diagnostic components contained within the Microgravity Science Glovebox (MSG) aboard the ISS is shown in Fig. 1a, and a cross-sectional view of the ZBOT-NC test tank inside its temperature-controlled vacuum jacket (VJ) is displayed in Fig. 1b. The test cell is machined and polished from optical quality cast acrylic. It consists of a cylindrical midsection which is capped at the two ends by hemispherical domes (4" in diameter by 8" in height). The tank is equipped with two strip heaters which are mounted circumferentially on the outer surface of the cylindrical acrylic wall. To provide containment, as well as definable and controllable thermal boundary conditions for CFD model validation, the test cell is thermally and physically isolated from the MSG environment via the vacuum jacket which is, in turn, enclosed within a cooling jacket. This cooling jacket, along with strip heaters placed at different locations on the outer surfaces of the vacuum jacket, allow the vacuum jacket to be controlled to designated experimental temperature levels. A nozzle is inserted

into the tank from the bottom hemispherical end, with its outlet plane positioned at a height aligned with the top of the strip heaters on the tank, for pressure control jet-mixing tests.

The tank self-pressurization tests are initiated with the tank at a uniform temperature, T_o. During these self-pressurization tests, the tank can be heated either locally by the tank strip heaters, or globally by the vacuum jacket; these simulate localized heat leaks conducted through the tank support structures or global heat leaks into a propellant tank from the surroundings, respectively. The pressure control tests can be initiated either after a self-pressurization test, when the tank is thermally stratified, or with the tank at a uniform elevated temperature T_o. During these pressure control tests, liquid is extracted from the tank, thermally conditioned to a subcooled temperature, T_{Jet}, which is below T_o, and pumped back into the tank through the nozzle. The initial tank fluid temperature, T_o, and the jet flow temperature, T_{Jet}, are maintained by careful conditioning of the fluid via a counter-flow shell and tube heat exchanger in the Fluid Supply Unit (FSU), which is located just below the vacuum jacket in the MSG.

The simulant phase change fluid used in this experiment is Perfluoro-n-Pentane (PnP, or C_5F_{12}). PnP is a non-polar volatile refrigerant with a boiling point of 29 ^{o}C at 1 atm. Its contact angle is close to zero degrees making it a near-perfect wetting fluid. Xenon is used as a noncondensable gas, simulating gaseous Helium which is commonly used to pressurize cryogenic propellant tanks. It is injected into the tank through the flow line in the FSU, and the system is then mixed continuously under isothermal conditions (at T_o) until the partial pressure of the vapor in the ullage plateaus to a constant level.

The simulation case studies that are presented in this section focus only on VJ self-pressurization where the tank is initially at T_o = 34 K, and the tank is heated globally by the VJ by maintaining its area-averaged temperature, T_{VJ}, at two degrees above the area-averaged tank temperature, T_{TW}, such that $T_{VJ} = T_{TW} + 2$ K. We will also concentrate on jet mixing pressure control tests where the tank starts at a uniformly elevated temperature, T_o = 38 K, and the jet temperature is set to a subcooled level of $T_{Jet} = T_o - 6$ K. For the one-component pure fluid cases, the molar concentration, x_g, of the noncondensable gas, xenon, is set to zero in the simulations. For the two-component cases, the molar concentration of xenon in the ullage is set to $x_g = 0.25$. The ZBOT-NC Experiment's geometry and configuration, displayed in Fig 1b, were adopted and meshed for the present CFD study. The nonuniform unstructured quad meshes that are used in the simulations are displayed in Fig 2.

CFD simulations for the 1g ground-based self-pressurization of the PnP tank with and without the noncondensable gas are presented first as displayed in Figs. 3-5. Here, the initial tank wall and fluid temperatures are uniformly at T_o = 34 K. The initial tank pressure is at its saturated value, P_o = 121.6614kPa. During self-pressurization, the tank is heated by the vacuum jacket, where the temperature of the vacuum jacket is maintained at $T_J = T_{TW} + 2$ K. The predicted evolutions of the tank temperature and flow patterns for the 1g self-pressurization of pure PnP ($x_g = 0$) are shown in Fig 3. The flow pattern indicates a relatively strong natural recirculation pattern in both the liquid and the vapor. These recirculating flows are created by the warmer liquid and vapor rising in the vicinity of the heated tank wall and descending in the central core region along the longitudinal axis of the tank. This natural convective flow promotes a vertical thermal stratification in both the vapor and the liquid. But the thermal stratification in the vapor seems to be stronger than in the liquid. As shown in Fig 4b, the tank pressure for the pure PnP case increases with time by roughly 16 kPa due to this stable 1g thermal stratification, as the warm liquid that is carried to the liquid-vapor interface by the natural convection flow promotes evaporation at the phase front. The

interfacial evaporative mass transfer for the pure system has a peak that occurs very early and decreases sharply by two orders of magnitude for the rest of the self-pressurization cycle, as indicated in Fig 4a. The time evolution of the fluid temperature at sensor RTF01is shown in Fig. 4c. This sensor is placed on the inner surface of the top tank wall dome, close to the central axis of the tank (see Fig 1b). The time evolution at RTF01 indicates that, for the pure system in 1g, the temperature of the vapor near the top of the tank rises by roughly 5 K during the 5 hour pressurization period. The temperature of a point at the center of the interface is also plotted in this figure as a rough indication of the extent of the vertical thermal stratification in the ullage region.

The predicted evolutions of the tank temperature and flow patterns for 1g VJ self-pressurization in the presence of the noncondensable gas in the ullage (with x_g = 0.25) are shown in Fig 5. A comparison of the recirculating flow and thermal stratification patterns for this case (with xenon) and its counterpart with a pure vapor (shown in Fig 3) indicates very minor differences. The distribution of xenon in the ullage is indicated by the molar concentration contours in Fig. 5. Due to the interfacial evaporation of the PnP, the concentration of xenon (or its partial pressure) in the ullage steadily decreases during self-pressurization. However, the distribution of xenon in the ullage seems to be quite uniform at all stages of self-pressurization due to the relatively strong natural convection recirculation in the ullage region. Fig 4a indicates that the integrated interfacial evaporative mass transfer rates for the pure and the noncondensable simulations are almost identical. The initial peak in the evaporation rate seems to be slightly decreased for the noncondensable case. However, the pressure evolution curves in Fig 4b indicates almost identical self-pressurization rates for the pure and noncondensable systems. Fig 4c indicates that in 1g the extent of the vertical thermal stratification of the two systems is also identical. These results suggest that the presence of the noncondensable gas does not have a major impact on 1g self-pressurization.

Next we consider microgravity VJ self-pressurization of the tank with and without the noncondensable gas, as displayed in Figs. 6-8. The evolutions of the flow and temperature fields for the pure system in microgravity are shown in Fig 6. An extremely weak recirculation flow still exists in the liquid due to the residual gravity, but conduction dominates over the weak residual natural convection in both the vapor and liquid regions. The thermal stratification in this case is in the transverse direction, as opposed to the vertical stratification in 1g. This microgravity thermal stratification is quite different from its 1g counterpart, exhibiting a roughly circular pattern that is evident in the liquid domain, with warmer liquid near the tank wall and colder liquid in the core region. In the absence of strong convection, the flow pattern in the ullage is mainly set by the interfacial evaporation-condensation process, with evaporation taking place at the upper interfacial regions close to the hot wall, and condensation occurring at the lower central interfacial region that is in closer contact with the cooler liquid core. Fig. 7a indicates that the net integrated interfacial mass transfer is also evaporative for the pure system in microgravity, and consequently the tank pressure rises by around 15 kPa during the self-pressurization interval of 4 hrs, as shown in Fig. 7b, which is slightly lower than its 1g counterpart. However, Fig. 7c shows that there is no vertical thermal stratification in the ullage in microgravity for the pure tank system in contrast to its 1g counterpart.

The predicted flow, temperature, and noncondensable concentration for microgravity VJ self-pressurization in the presence of the noncondensable gas in the ullage (x_g = .25) are shown in Fig

8. The evolution of the flow and temperature fields in this case are noticeably different compared to the pure system. Since evaporation still takes place at the top heated portion of the interface, while condensation ensues in the lower central interfacial section, there is a nonuniform distribution of vapor pressure along the wall, as indicated by the noncondensable mole fraction contours in Fig 8. This variation in the vapor pressure along the interfaces causes a non-uniform top to bottom interfacial temperature gradient that gives rise to a thermocapillary (Marangoni) convection. This thermocapillary convection drives the warm fluid along the interface from the upper sections near the wall to the lower section near the bottom of the interface. This thermocapillary flow is in the same direction as the residual natural convection flow which was also observed in the previous pure system. Therefore, it noticeably strengthens the recirculatory annular convective vortex in the liquid, as is evident from the flow patterns in Fig. 8. This type of thermocapillary flow seems to have been encountered previously, in the microgravity boiling experiment by Straub et al [10, 11], where a jet flow that emanated from a bubble on a heated wall was observed. This unexpected flow was attributed to thermocapillary convection caused by the noncondensable gases that were present in their fluid system and found their way into the bubble. As shown in Fig. 7a, the net integrated interfacial mass transfer rate in the ullage is still evaporative, but due to the cooling effect of the thermocapillary flow caused by the noncondensable gas, the net evaporative mass transfer rate is considerably decreased after its initial peak as compared to its pure system counterpart. The mitigated net evaporation rate also causes a noticeably lower tank self-pressurization rate for the noncondensable gas case as compared to the pure system, as shown in Fig 7b. There is, however, a small degree of vertical thermal stratification in the microgravity noncondensable case that is absent in its pure system counterpart, as shown in Fig. 7c.

To understand the intricate relationship between the partial pressure distributions in the vapor, the variation in the interfacial temperature, the induced thermocapillary flow, and the interfacial condensation-evaporation process during microgravity self-pressurization, it is useful to examine and compare the interfacial conditions for the pure and noncondensable systems. The molar concentration of vapor along the interface is plotted in Fig. 9a at different times for the microgravity noncondensable self-pressurization case. In these plots, the x-axis starts at the bottom of the ullage bubble and ends at its top. The molar concentration of vapor at the interface is uniform and equal to 1 along the interface during the entire self-pressurization for the pure system. However, Fig. 9a indicates that during the self-pressurization of the two-component system, the concentration of vapor drops near the lower center of the ullage where the vapor condenses, while the noncondensable gas accumulates in that region. However, the concentration of vapor increases in the upper portions of the interface near the wall, where evaporation takes place. Naturally, this figure also indicates that the average concentration of the vapor in the ullage increases during self-pressurization due to the net interfacial evaporation. Since the interfacial temperature is dictated by the vapor partial pressure, it is uniform along the interface for the pure vapor self-pressurization case, as shown in Fig. 9b. However, the noncondensable self-pressurization simulation indicates that an interfacial temperature gradient is created along the interface following the vapor pressure variation, with lower temperatures in the bottom center of the ullage and higher temperatures near the upper interface sections close to the tank wall. This temperature variation drives the thermocapillary flow from the hot upper interfacial section to the cold lower interfacial section, as

was observed in Fig. 8. The nominal and approximate magnitude for the maximum thermocapillary velocity that can potentially be generated by the predicted interfacial temperature gradient can be calculated from the scaled relationship below which is plotted in Fig. 9c.

$$U_{Marangoni} = \Gamma_T \frac{dT}{ds} \frac{R_{ullage}}{\mu_l} \tag{20}$$

It should be noted that this velocity was not predicted by the CFD simulation; rather, it is calculated as a maximum potential value from the relationship in Eq. (20).

Finally, the mass transfer rate predictions along the interface, plotted in Fig. 9d, indicate that for the microgravity noncondensable case, due to the cooling effect of the thermocapillary flow, the predicted condensing section of the interface increases in extent, while the predicted evaporating section decreases as time evolves, in comparison to the pure vapor case. This is the main cause of the decrease in the net evaporation mass transfer rate for the noncondensable case which results in a lower microgravity self-pressurization rate compared to the pure system.

The next case that is considered is pressure control of the ZBOT-NC tank using subcooled jet mixing in microgravity. The jet speed in these simulations is 4 cm/sec, while the jet temperature is set to be at $T_{Jet} = T_o - 6$ K, or 32 °C. The tank is initially at an elevated temperature of $T_o = 38$ °C. The jet Weber number for this case is around 0.35, thus, there is no penetration of the interface or geyser formation that would violate the assumption of the sharp rigid interface. Fig. 10 displays the evolution of the flow and temperature fields in the tank during microgravity jet mixing for the pure vapor system. Due to the drastically reduced buoyancy force in microgravity, the subcooled jet reaches the interface in less than 10 seconds. At around t = 900s, the subcooled jet has completely surrounded and cooled the ullage, promoting condensation at the lower hemispherical section of the interface, and by t = 1800s, the whole ullage is essentially at the subcooled jet temperature. The change in the integrated interfacial mass transfer rate with time during jet mixing for this pure system is plotted in Fig. 11a, and the tank pressure and temperature evolutions are included in Fig. 11b and 11c, respectively. The graphs indicate a very high initial condensation rate for the pure tank system which is accompanied by a rapid drop in the tank pressure as the jet impinges upon the ullage interface. The condensation rate gradually tapers down as the ullage pressure and temperature decrease and plateau. Fig. 11c indicates that as the jet impinges on the interface in the pure tank system, a large vertical temperature gradient is created in the ullage that gradually subsides during the cooling pressure control process.

The evolutions of the temperature, noncondensable gas concentration, and flow fields during depressurization of the two-component noncondensable tank system in microgravity are displayed in Fig. 12. As the subcooled jet impinges on the lower central section of the interface and promotes condensation of the vapor, the noncondensable gas accumulates and rises in the center of the ullage. However, at the upper sections of the interface near the hot wall, evaporation ensues, producing a flow of vapor into the ullage. In the presence of the noncondensable gas, this evaporation-condensation pattern produces a nonuniform distribution of vapor concentration (vapor partial pressure) along the interface. As described before, this variation in the partial pressure of the vapor gives rise to a thermocapillary flow that carries the fluid along the interface from the upper warmer interface sections near the wall towards the cooler bottom center section of the interface. During the pressure control process, this Marangoni flow opposes the jet flow along the interface and impedes it from engulfing the ullage as it did in the pure tank system. The multi-vortexed flow structure that is created at t = 1800s by the interaction between the

noncondensable gas-induced thermocapillary convection and the jet flow in microgravity is in sharp contrast to the subcooled jet flow that surrounds and engulfs the ullage in the pure tank system. In the two-component tank system, there are two mechanisms that impede condensation. First, the accumulation of noncondensable gas at the phase front produces a transport barrier that impedes the vapor from getting to the interface to condense. Second, the thermocapillary vortex created by the noncondensable gas effect prevents the subcooled jet from cooling the interface/ullage as readily and easily as it does in the pure system. Both of these phenomena are shown clearly in the flow and concentration fields displayed in Fig. 12. The impact of the transport and flow resistance created by the noncondensable gas on the integrated interfacial mass transfer and tank pressure are indicated in Fig. 11a and 11b, respectively. Fig. 11a shows that the net integrated interfacial condensation rate for the noncondensable gas case is severely reduced compared to the pure system, especially at the start of the jet flow. Consequently, the predicted rate of tank depressurization by the subcooled jet flow is also drastically reduced for the noncondensable case compared to the pure vapor case in microgravity, as indicated in Fig. 11b. Finally, the extent of the vertical stratification that is created in the ullage during microgravity depressurization is noticeably larger in the presence of noncondensable gas in the ullage in comparison to the pure tank system.

The intricate interfacial interactions that are responsible for the different pressure reduction behaviors during jet mixing in microgravity with and without the noncondensable gas are presented in Fig. 13. While the molar concentration of vapor at the interface is uniform and equal to 1 along the entire interface for the pure tank system during the microgravity jet mixing interval, its value changes greatly along the interface for the two component system, as evident in Fig. 13a. Because the subcooled jet produces significant condensation at the point of impingement near the center of the ullage interface, the vapor concentration drops while the noncondensable gas accumulates in this lower central interface region. Initially, at t = 30s, this produces a severe nonuniformity in the molar concentration of the vapor (or the vapor partial pressure) along the interface. This predicted nonuniformity tends to reduce with time as convective mixing uniformizes the partial pressure of the vapor in the ullage. The impact of the variation of the vapor partial pressure on the interface temperature is displayed in Fig. 13b. First, we will examine the interfacial temperature variation for the pure system. Here, it is seen that the interface temperature is uniform at its saturation value all along the upper portion of the interface where the mass transfer is due to evaporation, but interestingly, it deviates from its saturation value where the subcooled jet impinges on the interface and the relatively large condensing mass transfer that ensues drives the interface away from a near equilibrium condition. In the case with the noncondensable gas, the interfacial condensation mass transfer is mitigated. Here, the interface temperature that is dictated by the nonuniform vapor partial pressure variations in the ullage also varies drastically along the interface, with a large decline at the point of jet impingement. As time goes on, the temperature gradient along the interface exhibits several sign reversals which follow the vapor partial pressure variations in the ullage. These changes in the interfacial temperature gradient ultimately lead to the multi-vortexed flow structure near the interface that is displayed in Fig. 12; this structure is brought about by the intricate interactions between the jet flow and the interfacial thermocapillary convection. Fig. 13c indicates that both the predicted condensing and evaporating mass transfer rates along the lower and upper portions of the interface, respectively, are noticeably

mitigated for the two-component system due to the transport and flow resistances instigated by the noncondensable gas in comparison to the pure tank system. As time ensues, the condensation and evaporation rates for both the pure and noncondensable systems continue to decrease along the interface; however, the condensation rate for the noncondensable tank system always remains noticeably mitigated compared to the pure tank case.

Finally, it is informative to make a direct comparison between the depressurization behavior of the pure and two component systems in 1g. Due to buoyancy effects, the 4 cm/s subcooled jet has difficulty reaching the interface in a reasonable amount of time. Therefore, we will first examine a subcooled jet mixing case in 1g where the jet velocity is increased to 10 cm/sec, while the jet temperature and the initial elevated tank temperature remain as before. The evolutions of the flow and temperature fields for the pure system are examined first. Fig. 14 indicates that it takes around 1000s for the jet to reach the interface in 1g due to the opposing buoyancy force. Here, in contrast to the microgravity case, as the subcooled jet gradually overcomes the buoyancy force and approaches the interface, it mixes and cools all of the liquid around it. Thus, in effect, it creates a rather planar cold front that gradually reaches the interface at around 1000s. This behavior is quite different from its microgravity counterpart, which is shown in Fig. 17.

Jet mixing depressurization of the two component noncondensable system is considered next. Fig 15 indicates that the jet mixing flow pattern in 1g for the noncondensable case is almost the same as in the pure system. The time for the jet to get to the interface is also almost the same as for the pure vapor case. However, when the noncondensable gas is present in the ullage, an interesting phenomenon occurs in the ullage region in 1g that is not observed in microgravity. When the subcooled jet impinges on the interface and condensation of the vapor ensues, the noncondensable gas, xenon, accumulates in the ullage region around the center of the flat interface. Although the cooled xenon in this region is in a stable thermal condition in 1g, it is under an unstable solutal condition since it is much lighter than PnP. As a result, a solutal convective flow ensues that carries the cooler xenon up along the central axis of the tank towards the warmer upper region of the ullage. This situation can be sustained as long as the condensation process promoted by the subcooled jet sustains the noncondensable gas rise. However, at around t = 1200s (~20 mins), as the condensation rate declines with time and the solutal convection becomes weaker, the unstable presence of cold xenon gas in the warm ullage vapor region cannot be sustained and thermal convection takes over, bringing the cold noncondensable gas back to the interface region, as shown at t = 1500 secs in Fig. 15. Thus, as a result of the double diffusive convection caused by the presence of noncondensable gas, a thermal inversion takes place in the ullage region that uniformizes the temperature and partial pressures in the ullage region in 1g.

Fig. 16a indicates that the net integrated interfacial mass transfer rate is condensing throughout the subcooled jet mixing interval for both the pure vapor and the noncondensable gas systems in 1g. The peak condensation rates for both cases occur after the subcooled jet impinges upon the interface at around t = 960s (16 min). It is also evident that, during the 1g jet mixing, the peak condensation rate is noticeably smaller for the noncondensable case compared to the pure vapor system. The evolutions of tank pressure with time during 1g mixing for the pure and noncondensable tank systems are shown in Fig. 16b. The pressure histories indicate that the delay time for the pressure drop to occur is the same for both cases. However, the rate of the pressure drop is lower for the case with noncondensable gas than for the pure system. Since, in 1g, the jet

flow pattern is hardly affected by the presence of a noncondensable gas, the decline in the interfacial condensation rate and the accompanying reduced depressurization rate for the noncondensable system are largely attributed to the transport resistance created by the presence of the noncondensable gas in the ullage.

Fig. 16c shows the predicted temperature history of a point at the top of the ullage at sensor location RTF01. For the pure system, this temperature declines monotonically after the initial delay. However, for the noncondensable gas case, this temperature declines more rapidly after the initial delay, but at around 20 min, it rises rapidly and then declines again, due to the thermal inversion that is instigated by the double-diffusive convection. It is also interesting to note that after the jet impinges the interface, the pressure curves for the pure and noncondensable tanks displayed in Fig. 16b continue to be on top of each other until the thermal inversion occurs at t = 20 mins. This is because, in 1g, the solutal convection initially removes the noncondensable gas from the vicinity of the interface, allowing the pure vapor to reach the interface without any transport barrier. However, once the thermal inversion occurs in the ullage, the noncondensable gas mixes throughout the ullage domain, and the transport resistance it creates near the interface reduces the depressurization rate for the noncondensable tank system compared to the pure vapor case.

Finally, the results of the microgravity jet mixing simulations at the higher jet velocity of 10 cm/sec are displayed in Figs. 17 through 19 for direct comparison with both the microgravity jet mixing case with the lower jet velocity, and with the previously described 1g jet mixing case at 10 cm/s. It should be mentioned that, for this jet velocity, the Weber number for the jet is slightly above the critical Weber number for geyser formation. Thus, in reality, a very small deformation of the interface might be expected at this jet velocity in microgravity which is not captured by the sharp interface CFD model. The flow pattern in Fig. 17 indicates that the higher jet velocity of 10 cm/s can to some extent overcome and diminish the microgravity thermocapillary vortices that were prominent in the flow patterns for the lower jet velocity of 4 cm/s, as displayed in Fig. 12. A comparison between the microgravity jet mixing results at 10 cm/s in Figs. 19a and 19b with the results of its 1g counterpart in Figs. 16a and 16b indicates that the impact of noncondensable gas in reducing the condensation and depressurization rates is still more prominent in microgravity than in 1g, even at a jet velocity of 10 cm/s. A comparison between Fig. 16c and Fig. 19c underscores the fact that the thermal inversion which occurs in 1g for the noncondensable gas due to the double-diffusive convection is absent in microgravity due to the reduced buoyancy force.

Conclusion

The Zero-Boil-Off Tank-Noncondensable (ZBOT-NC) Experiment is being developed to study the effects of a noncondensable gas on self-pressurization and jet mixing pressure control of a volatile fluid in 1g and microgravity, with applications to cryogenic fluid management of propellant tanks on the ground and in space. In this paper, a two-phase two-component Sharp Interface SI-CFD model is presented that was developed to aid the design of the ZBOT-NC Experiment and its microgravity text matrix. In the near future, this model will be validated against the microgravity data that will be collected during the ISS experiment. The model solves the Navier Stokes and continuity equations for fluid velocities and the energy and species equations for the temperature and molar concentrations, or partial pressures, of the vapor and noncondensable gas in the ullage. Numerical simulations performed by the axisymmetric SI-CFD model predict that the noncondensable gas can impact both self-pressurization and pressure control of a propellant

tank in 1g and microgravity by creating a transport barrier in the ullage that reduces interfacial condensation, as well as by instigating an interface-driven Marangoni or thermocapillary flow that alters the fluid and thermal structures in the vicinity of the ullage.

These numerical simulations indicate that the impact of a noncondensable gas on 1g self-pressurization is minimal and inconsequential. However, in microgravity, the CFD predictions indicate that the noncondensable gas can considerably reduce the rate of self-pressurization brought about by the global heating of the tank. This impact is caused more by the Marangoni effect on the liquid side than by the transport resistance inside the ullage.

The computational study also indicates that the noncondensable gas can have a considerable impact on tank depressurization by subcooled jet mixing in both 1g and microgravity. In 1g, the impact is mostly due to the transport resistance created in the ullage by the noncondensable gas that decreases the interfacial condensation rate and thereby the tank depressurization rate. A thermal inversion in the ullage caused by double-diffusive convection in 1g uniformizes the partial pressure variation along the interface, which minimizes the Marangoni effect.

The NCG effects on depressurization are more significant in microgravity than in 1g. Due to the weakened buoyancy force, the subcooled jet reaches the interface with almost no delay, but, due to the simultaneous effects of transport resistance in the ullage created by the noncondensable gas and the diversion of the subcooled jet flow by the Marangoni convection, which is also instigated by the noncondensable gas, there is a significant decline in both the interfacial condensation and tank depressurization rates compared to the pure vapor tank system.

Acknowledgements

Supported by the NASA Biological & Physical Sciences (BPS) Division, Physical Sciences Research Program, NASA HQ, and NASA Space Technology Mission Directorate (STMD), Cryogenic Portfolio Program, NASA GRC.

References

1. Othmer DF (1929) The condensation of steam, Indus. Eng. Chem. 21, pp 577-583.
2. Huang, J., Zhang, J., & Wang, L. (2015). Review of vapor condensation heat and mass transfer in the presence of non-condensable gas. Applied Thermal Engineering, 89, 469-484.
3. Minkowycz WJ, Sparrow EM (1966) Condensation heat transfer in the presence of noncondensables, interfacial resistance, superheating, variable properties, and diffusion, Int. J. Heat Mass Transfer 9 (10) 1125-1144.
4. Sparrow EM, Minkowycz WJ, Saddy M (1967) Forced convection condensation in the presence of noncondensables and interfacial resistance, Int. J. Heat Mass Transfer 10 (12) 1829-1845.
5. Colburn AP, Hougen OA (1934) Design of cooler condensers for mixture of vapors with noncondensing gases, Ind. Eng. Chem. 26 pp.1178-1182.
6. Kageyama T, P.F. Peterson PF, Schrock VE (1993) Diffusion layer modeling for condensation in vertical tubes with noncondensable gases, Nucl. Eng. Des. 141 (1-2) 289-302.
7. Peterson PF (2000) Diffusion layer modeling for condensation with multicomponent noncondensable gases, J. Heat Transfer, Vol. 4, pp716-720.

8. Revankar ST, Pollock D (2005) Laminar film condensation in a vertical tube in the presence of noncondensable gas, Appl. Math. Model. 29 (4) pp. 341-359.
9. Panzarella CH, Kassemi M (2009a) Analysis of Noncondensable Gas Effects on Evaporative and Condensive Mass Transfer Across a Liquid Vapor Interface, International Journal of Heat and Mass Transfer, Vol. 52, pp. 3767-3777.
10. Straub J (2001) Boiling heat transfer and bubble dynamics. Advances in Heat Transfer, 35, J.P. Hartnett, T.F. Irvine, Y.I. Cho & G.A. Greene, Eds. Academic Press, New York.
11. Straub J, (2002) Origin and effect of thermocapillary convection in subcooled boiling observations and conclusions from experiments performed at microgravity, Ann. N.Y. Acad. Sci. 974: 348–363.
12. Balasubramaniam R, Ramé E (2018) Condensation of a Quiescent Vapor by a Stagnation-Point Liquid Flow, Journal of Heat Transfer, Vol 140, No 5, 051501/1-10.
13. Bullard, B. (1972). Liquid propellant thermal conditioning system test program final report. NASA CR-72971.
14. Haba D, Himeno T, Watanabe T, Inoue C, Uzawa S, (2016) Experimental Study on Sloshing with Phase Change using Liquid Nitrogen, SP2016_3125342, Space Propulsion Conference Rome, Italy, May 4.
15. M. Kassemi, O. Kartuzova, S. Hylton, Validation of Two-Phase CFD Models for Propellant Tank Self-Pressurization: Crossing Fluid Types, Scales, and Gravity Levels, Cryogenics Vol. 89 pp. 1–15, Jan 2018.
16. Schrage, R, (1953) “A Theoretical Study of Interphase Mass Transfer,” Columbia University Press, New York.
17. M. Kassemi, O. Kartuzova, S. Hylton, Validation of Two-Phase CFD Models for Propellant Tank Self-Pressurization: Crossing Fluid Types, Scales, and Gravity Levels, Cryogenics Vol. 89 pp. 1–15, Jan 2018.
18. Brigham Young University, (2009) "DIPPR 801 Evaluated Process Data," BYU-DIPPR Thermophysical Properties Laboratory, Provo, UT.

List of Figures

interface (c), during microgravity subcooled jet mixing pressure control of the pure vapor and noncondensable tank systems: V_{Jet} = 4 cm/s, $T_{Jet} = T_0$ - 6 K, x_{xenon}= 0 and 0.25, FL= 65%.

Figure 12. Effect of noncondensable gas on the evolution of test tank temperature, noncondensable molar concentration, and flow fields during microgravity subcooled jet mixing pressure control of the two-component noncondensable tank system: V_{Jet} = 4 cm/s, $T_{Jet} = T_0$ - 6 K, x_{xenon}= 0.25, FL= 65%.

Figure 13. Effect of noncondensable gas on the variation of the molar concentration of vapor (a), interface temperature (b), and interfacial mass transfer rate (c), along the liquid-vapor interface at different times during the microgravity subcooled jet mixing pressure control test: V_{Jet} = 4 cm/s, $T_{Jet} = T_0$ - 6 K, x_{xenon}= 0 and 0.25, FL= 65%.

Figure 14. Predicted evolution of test tank temperature and flow fields during 1g subcooled jet mixing pressure control of the pure vapor one-component tank system: V_{Jet} = 10 cm/s, $T_{Jet} = T_0$ - 6 K, x_{xenon}= 0, FL= 65%.

Figure 15. Effect of noncondensable gas on the evolution of test tank temperature, noncondensable molar concentration, and flow fields during 1g subcooled jet mixing pressure control of the two-component noncondensable tank system: V_{Jet} = 10 cm/s, $T_{Jet} = T_0$ - 6 K, x_{xenon}= 0, FL= 65%.

Figure 16. Comparison of the predicted evolution of the integrated interfacial mass transfer rate (a), test tank ullage pressure (b), and temperature at location RTF01 and at a point at the center of the interface (c), during 1g subcooled jet mixing pressure control of the pure vapor and noncondensable tank systems: V_{Jet} = 10 cm/s, $T_{Jet} = T_0$ - 6 K, x_{xenon}= 0 and 0.25, FL= 65%.

Figure 17. Predicted evolution of test tank temperature and flow fields during microgravity subcooled jet mixing pressure control of the pure vapor one-component tank system: V_{Jet} = 10 cm/s, $T_{Jet} = T_0$ - 6 K, x_{xenon}= 0, FL= 65%.

Figure 18. Effect of noncondensable gas on the evolution of test tank temperature, noncondensable molar concentration, and flow fields during microgravity subcooled jet mixing pressure control of the two-component noncondensable tank system: V_{Jet} = 10 cm/s, $T_{Jet} = T_0$ - 6 K, x_{xenon}= 0, FL= 65%.

Figure 19. Comparison of the predicted evolution of the integrated interfacial mass transfer rate (a), test tank ullage pressure (b), and temperature at location RTF01 and a point at the center of the interface (c), during microgravity subcooled jet mixing pressure control of the pure vapor and noncondensable tank systems: V_{jet} = 10 cm/s, $T_{Jet} = T_0$-6K, x_{xenon} = 0 and 0.25, FL = 65%.

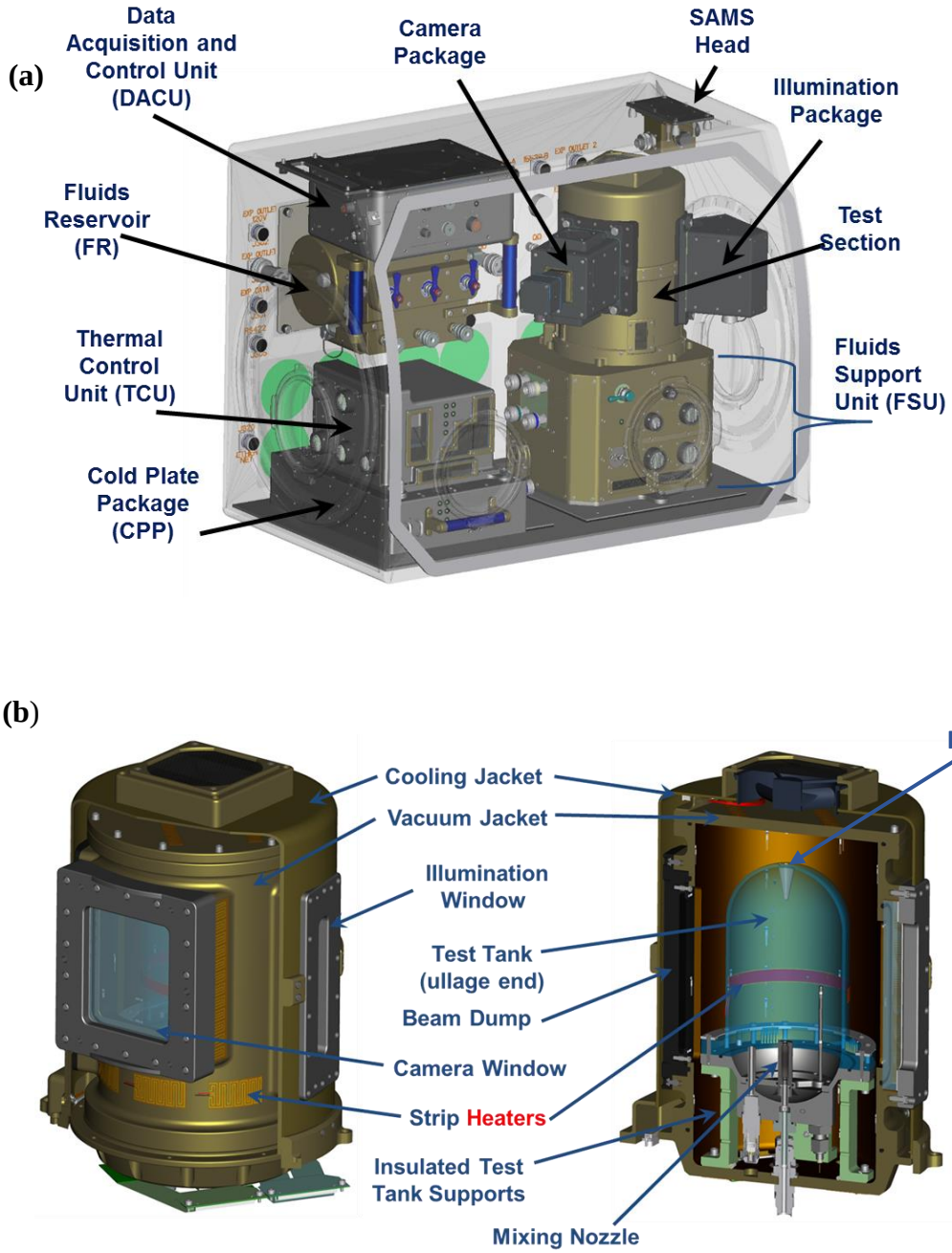
(a)
Data Acquisition and Control Unit (DACU)
Camera Package
SAMS Head
Illumination Package
Fluids Reservoir (FR)
Test Section
Thermal Control Unit (TCU)
Fluids Support Unit (FSU)
Cold Plate Package (CPP)
(b)
RTF01
Cooling Jacket
Vacuum Jacket
Illumination Window
Test Tank (ullage end)
Beam Dump
Camera Window
Strip Heaters
Insulated Test Tank Supports
Mixing Nozzle

Figure 1

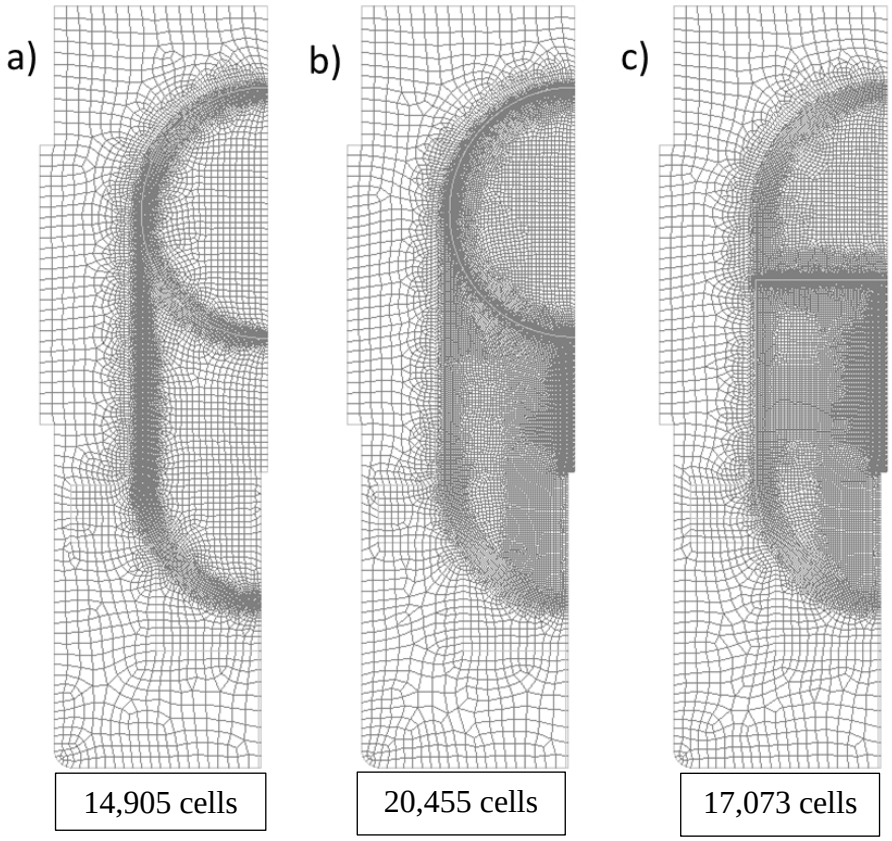

Figure 2

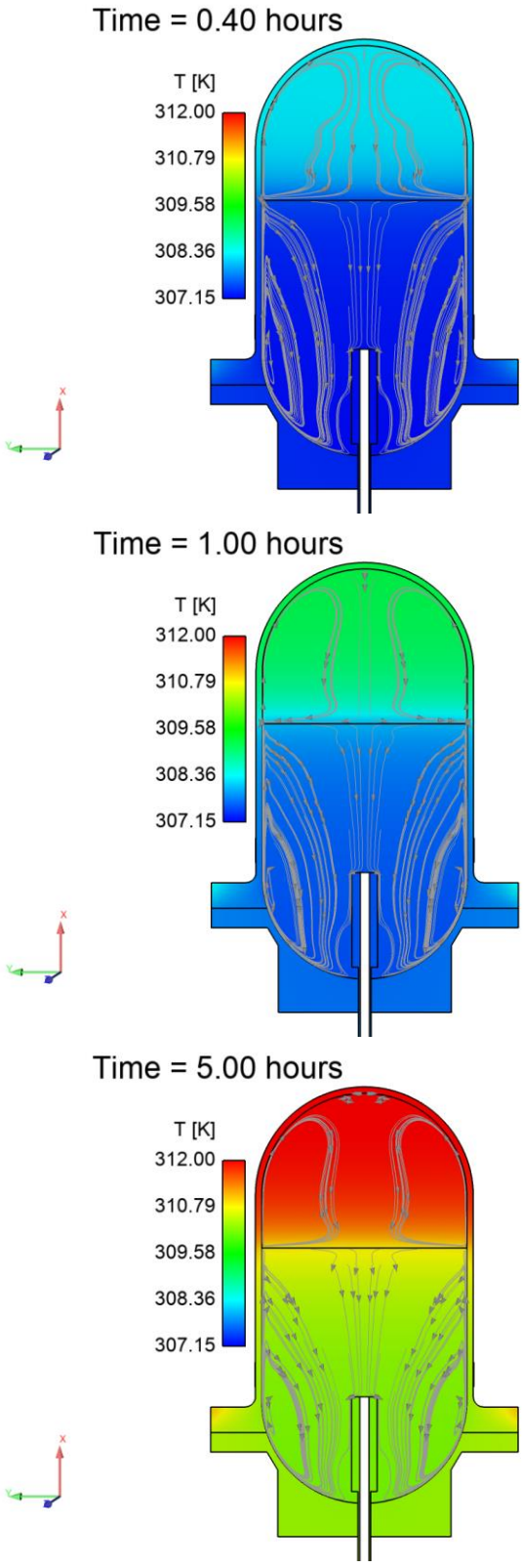
Time = 0.40 hours
T [K]
312.00
310.79
309.58
308.36
307.15
Time = 1.00 hours
T [K]
312.00
310.79
309.58
308.36
307.15
Time = 5.00 hours
T [K]
312.00
310.79
309.58
308.36
307.15

Figure 3

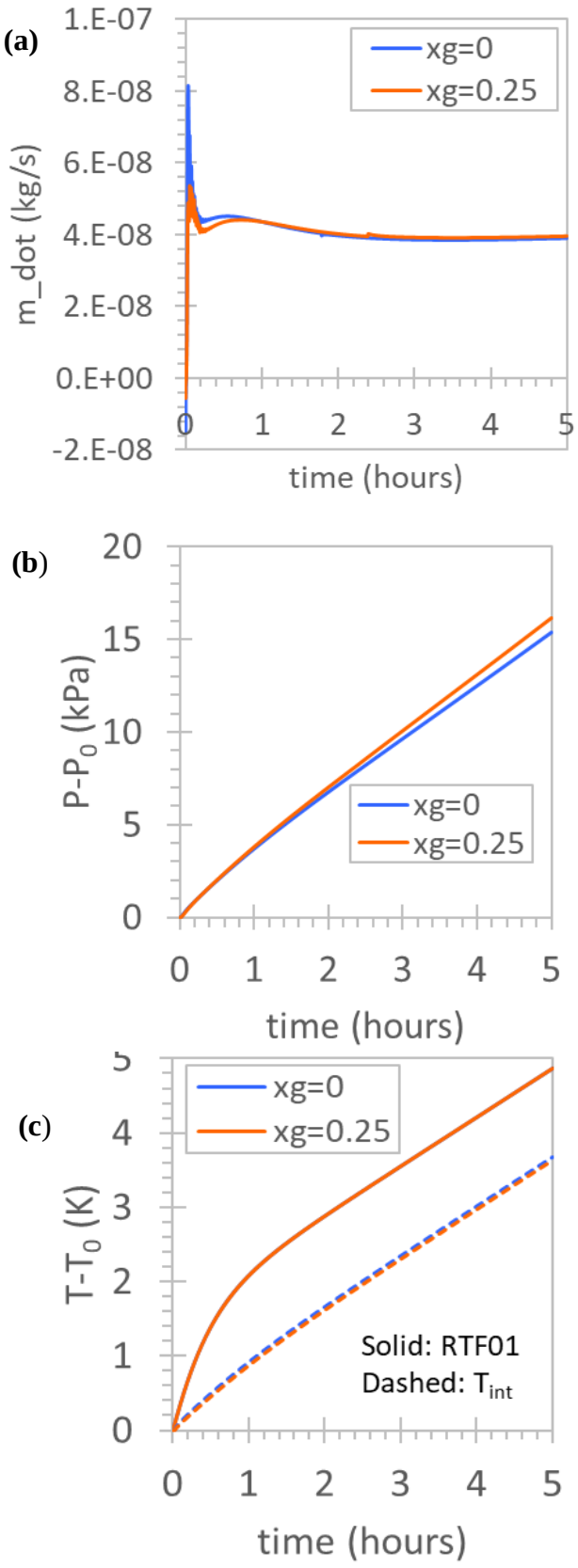
(a)
1.E-07
8.E-08
6.E-08
4.E-08
2.E-08
0.E+00
-2.E-08
m_dot (kg/s)
xg=0
xg=0.25
0
1
2
3
4
5
time (hours)
(b)
20
15
10
5
0
P-P0 (kPa)
xg=0
xg=0.25
0
1
2
3
4
5
time (hours)
(c)
5
4
3
2
1
0
T-T0 (K)
xg=0
xg=0.25
Solid: RTF01
Dashed: Tint
0
1
2
3
4
5
time (hours)

Figure 4

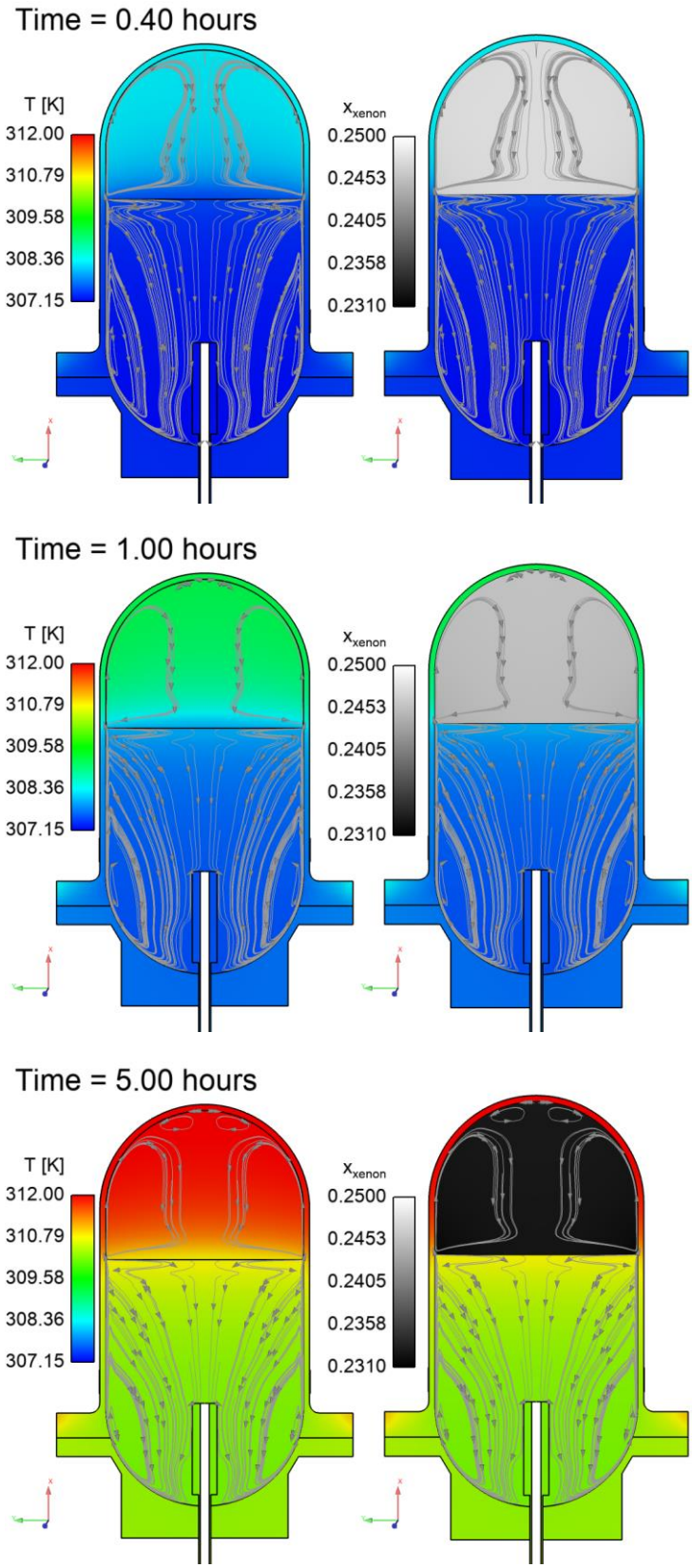
Time = 0.40 hours
T [K]
312.00
310.79
309.58
308.36
307.15
x_xenon
0.2500
0.2453
0.2405
0.2358
0.2310
Time = 1.00 hours
T [K]
312.00
310.79
309.58
308.36
307.15
x_xenon
0.2500
0.2453
0.2405
0.2358
0.2310
Time = 5.00 hours
T [K]
312.00
310.79
309.58
308.36
307.15
x_xenon
0.2500
0.2453
0.2405
0.2358
0.2310

Figure 5

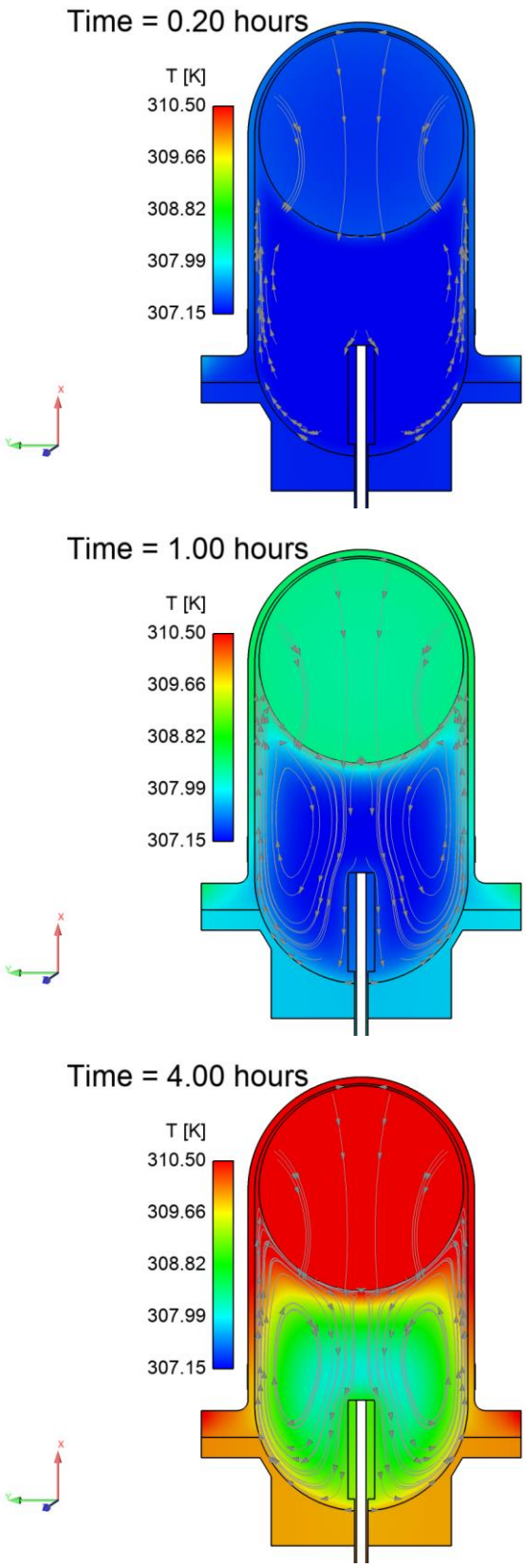
Time = 0.20 hours
T [K]
310.50
309.66
308.82
307.99
307.15
Time = 1.00 hours
T [K]
310.50
309.66
308.82
307.99
307.15
Time = 4.00 hours
T [K]
310.50
309.66
308.82
307.99
307.15

Figure 6

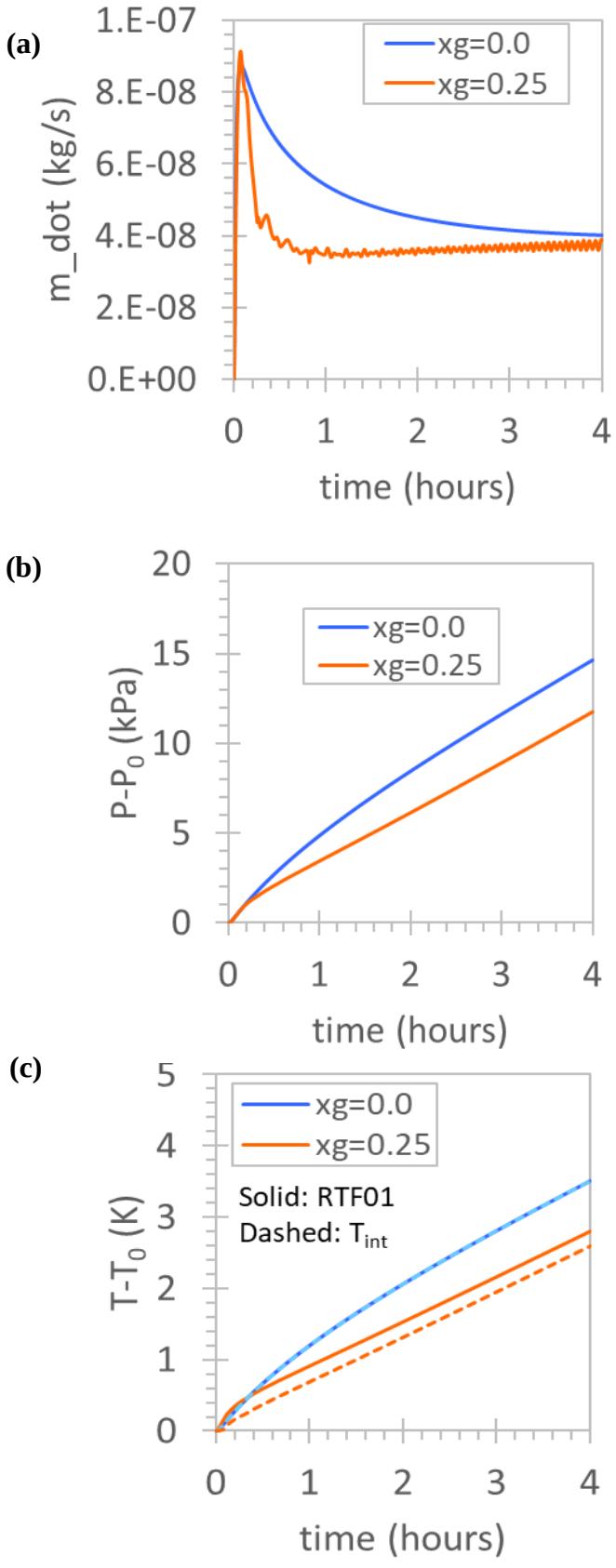
(a)
1.E-07
8.E-08
6.E-08
4.E-08
2.E-08
0.E+00
m_dot (kg/s)
xg=0.0
xg=0.25
0
1
2
3
4
time (hours)
(b)
20
15
10
5
0
P-P0 (kPa)
xg=0.0
xg=0.25
0
1
2
3
4
time (hours)
(c)
5
4
3
2
1
0
T-T0 (K)
xg=0.0
xg=0.25
Solid: RTF01
Dashed: Tint
0
1
2
3
4
time (hours)

Figure 7

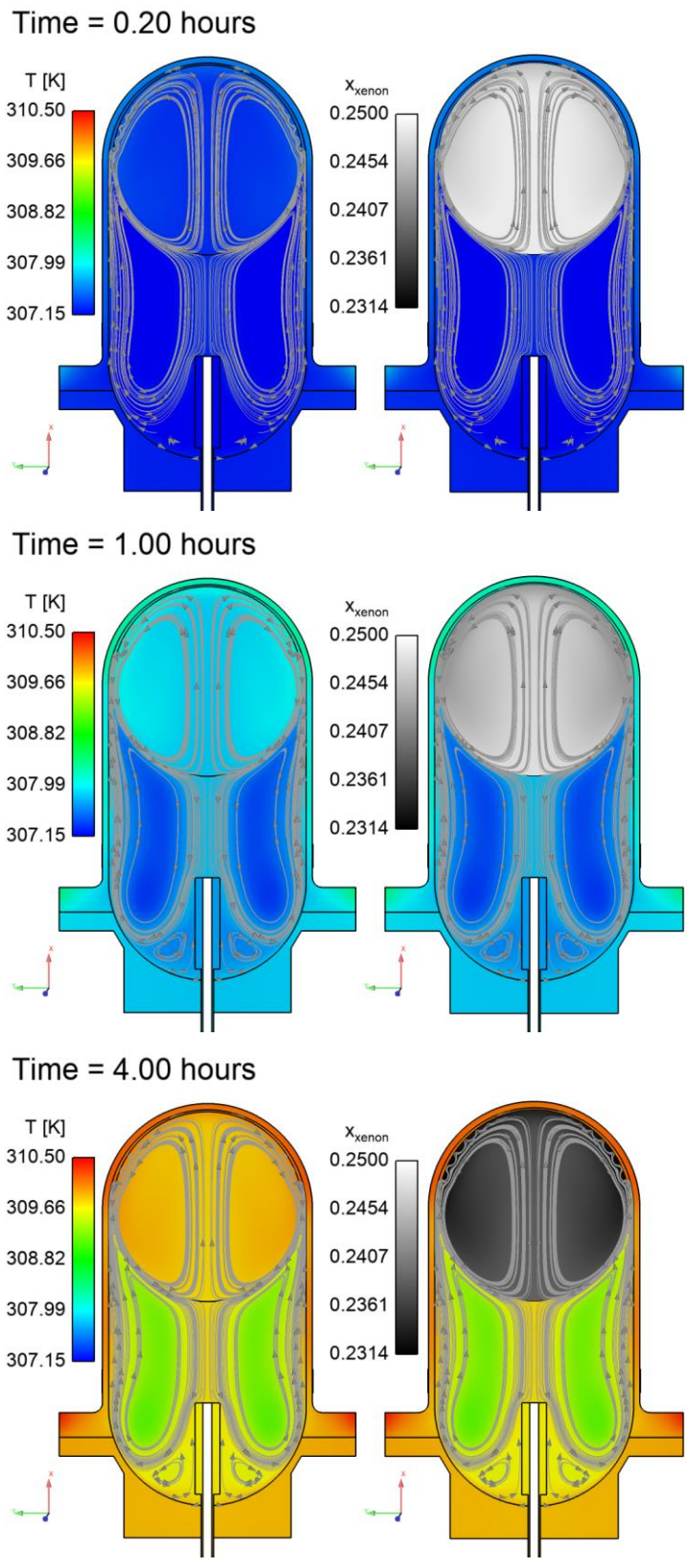
Time = 0.20 hours
T [K]
310.50
309.66
308.82
307.99
307.15
x_xenon
0.2500
0.2454
0.2407
0.2361
0.2314
Time = 1.00 hours
T [K]
310.50
309.66
308.82
307.99
307.15
x_xenon
0.2500
0.2454
0.2407
0.2361
0.2314
Time = 4.00 hours
T [K]
310.50
309.66
308.82
307.99
307.15
x_xenon
0.2500
0.2454
0.2407
0.2361
0.2314

Figure 8

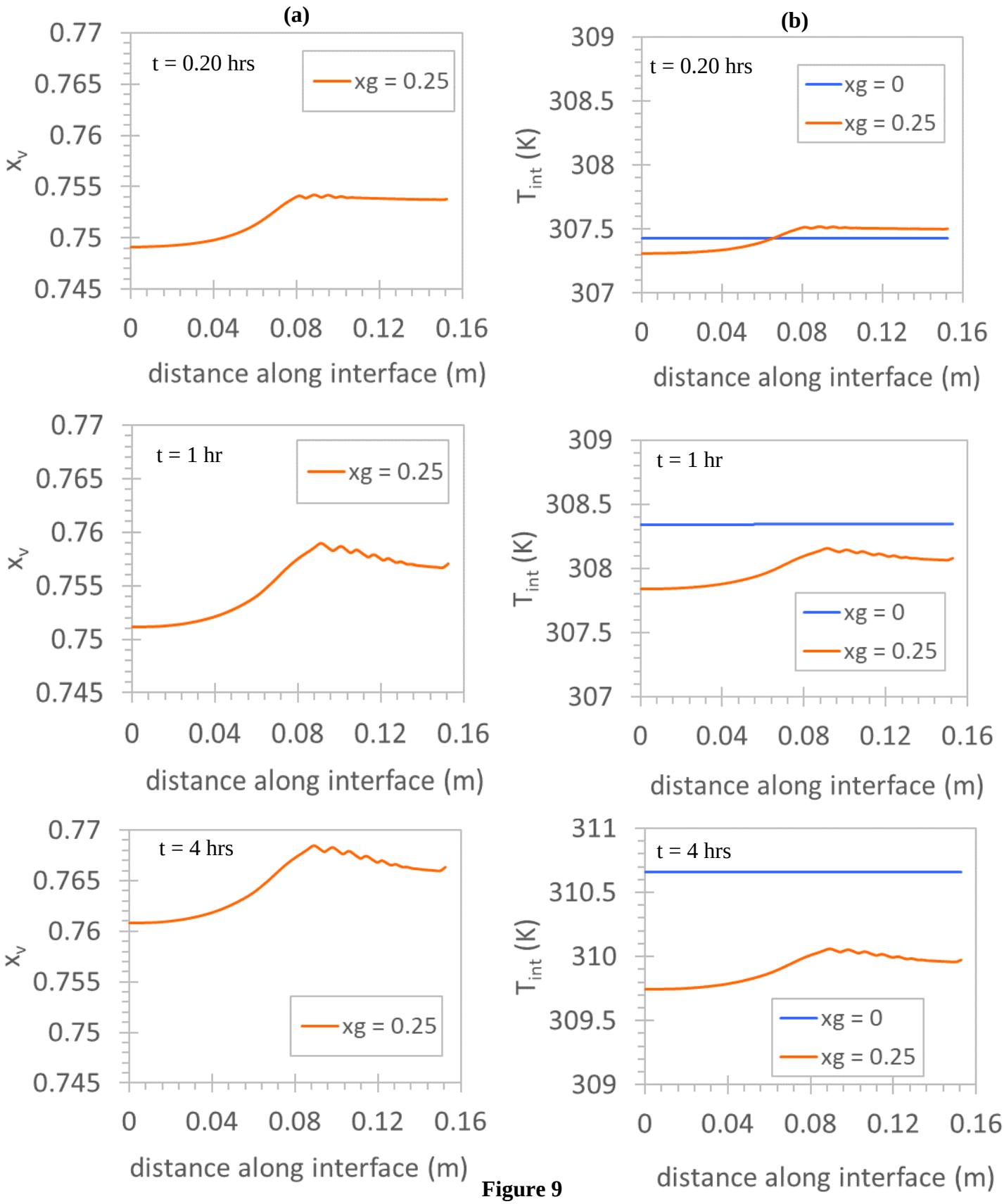
(a)
(b)
t = 0.20 hrs
xg = 0.25
x_v
0.77
0.765
0.76
0.755
0.75
0.745
0
0.04
0.08
0.12
0.16
distance along interface (m)
t = 0.20 hrs
xg = 0
xg = 0.25
T_{int} (K)
309
308.5
308
307.5
307
0
0.04
0.08
0.12
0.16
distance along interface (m)
t = 1 hr
xg = 0.25
x_v
0.77
0.765
0.76
0.755
0.75
0.745
0
0.04
0.08
0.12
0.16
distance along interface (m)
t = 1 hr
xg = 0
xg = 0.25
T_{int} (K)
309
308.5
308
307.5
307
0
0.04
0.08
0.12
0.16
distance along interface (m)
t = 4 hrs
xg = 0.25
x_v
0.77
0.765
0.76
0.755
0.75
0.745
0
0.04
0.08
0.12
0.16
distance along interface (m)
t = 4 hrs
xg = 0
xg = 0.25
T_{int} (K)
311
310.5
310
309.5
309
0
0.04
0.08
0.12
0.16
distance along interface (m)

Figure 9

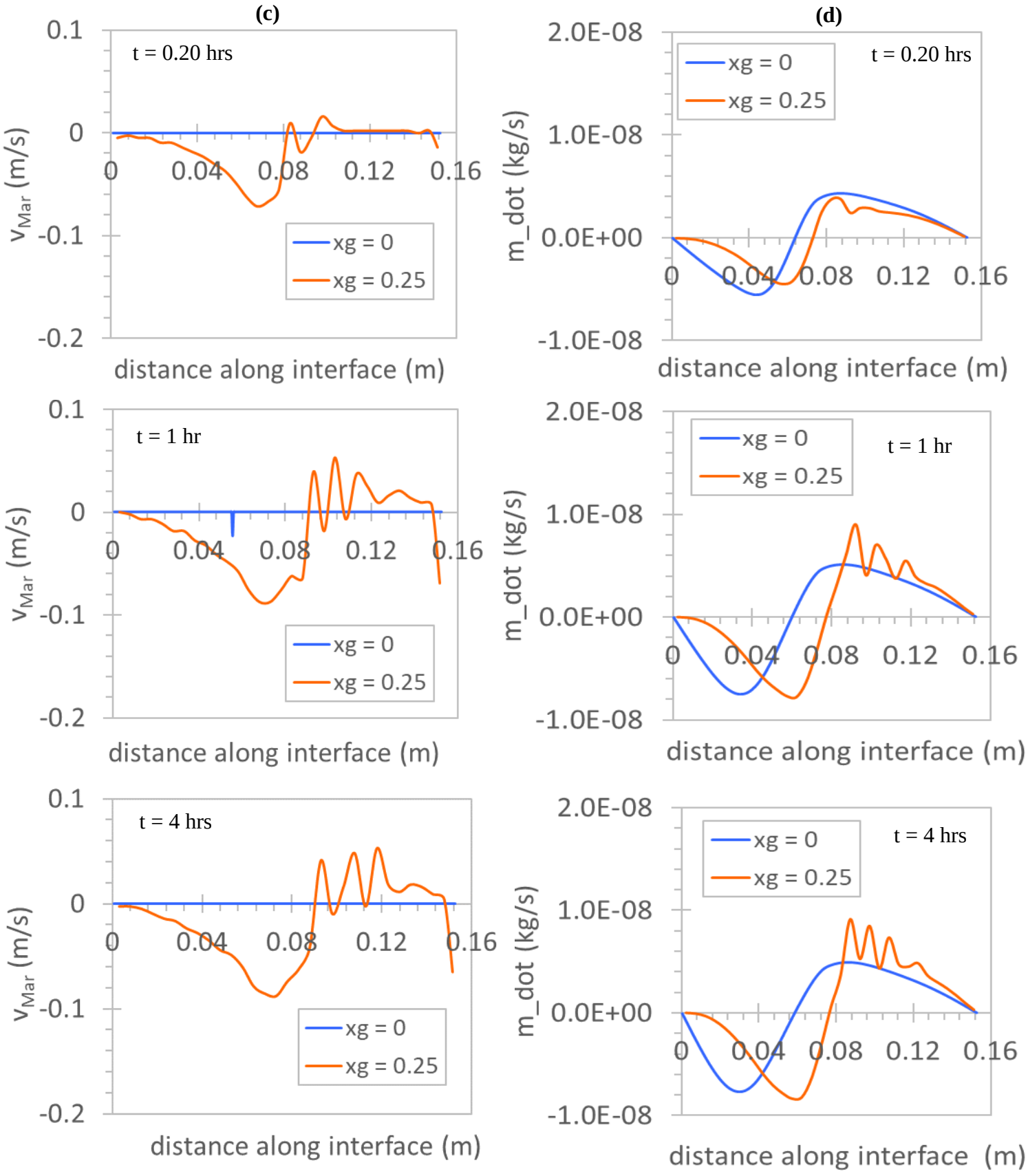

Figure 9 (continued)

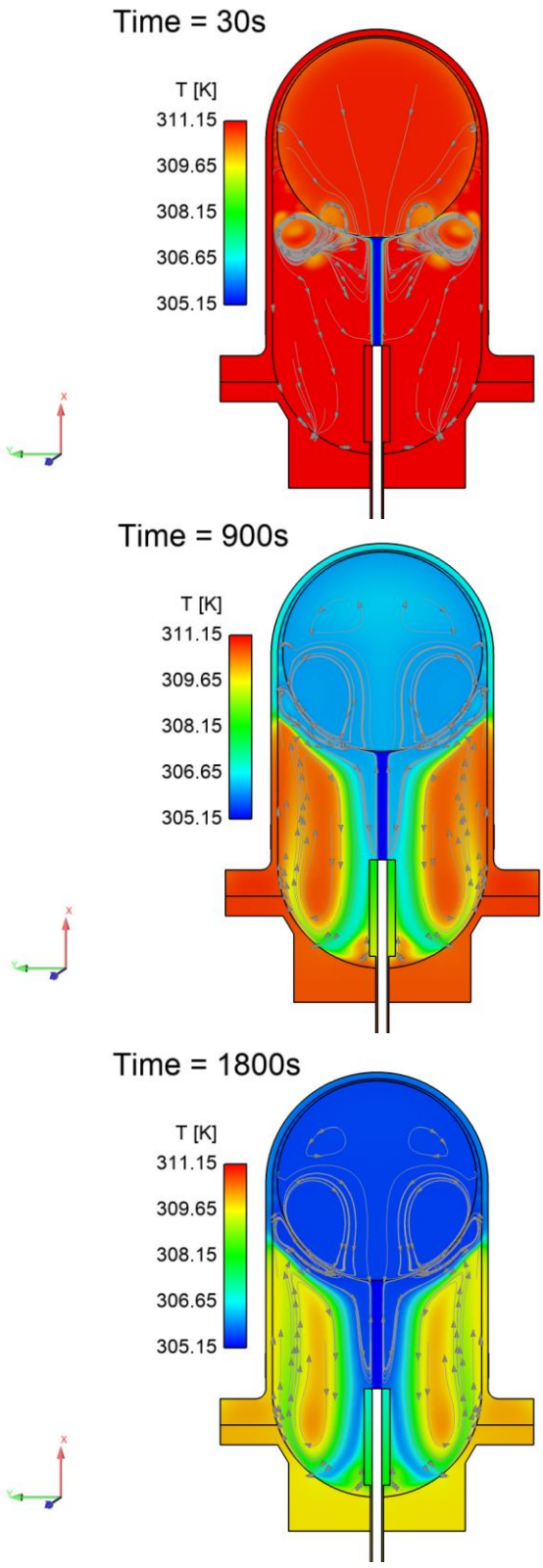
Time = 30s
T [K]
311.15
309.65
308.15
306.65
305.15
Time = 900s
T [K]
311.15
309.65
308.15
306.65
305.15
Time = 1800s
T [K]
311.15
309.65
308.15
306.65
305.15

Figure 10

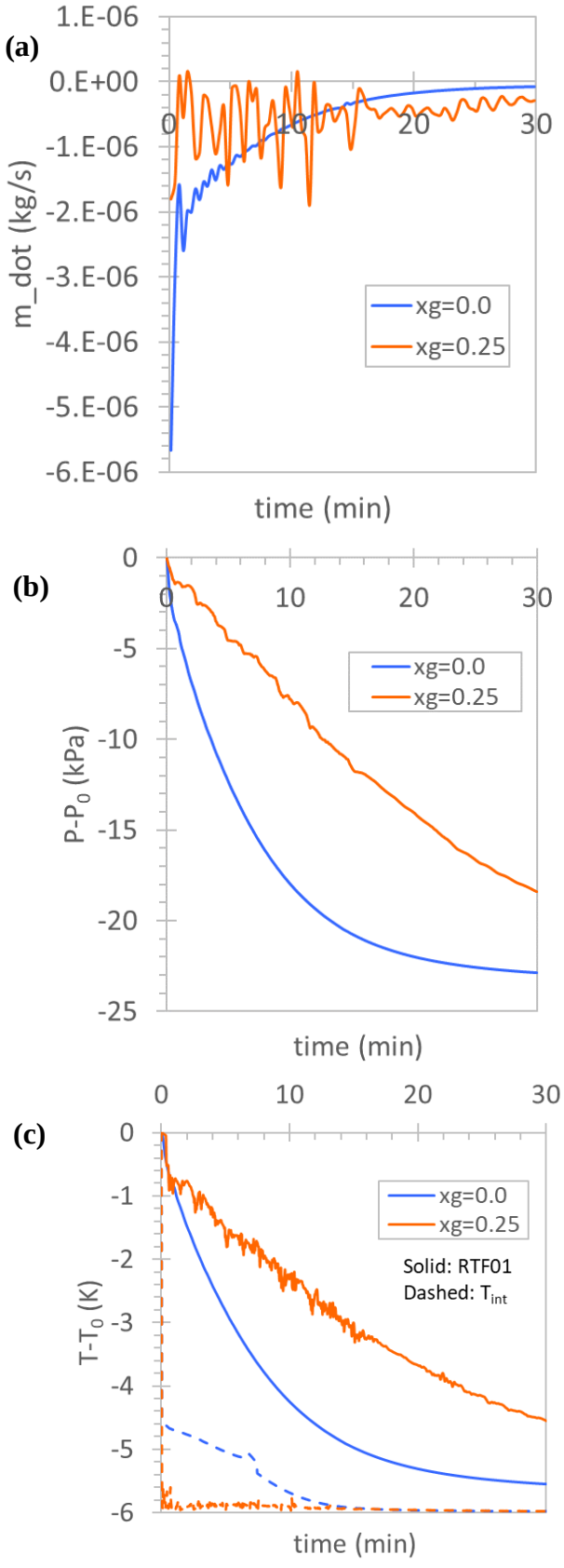
(a)
1.E-06
0.E+00
-1.E-06
-2.E-06
-3.E-06
-4.E-06
-5.E-06
-6.E-06
m_dot (kg/s)
0
10
20
30
time (min)
xg=0.0
xg=0.25
(b)
0
-5
-10
-15
-20
-25
P-P0 (kPa)
0
10
20
30
time (min)
xg=0.0
xg=0.25
(c)
0
-1
-2
-3
-4
-5
-6
T-T0 (K)
0
10
20
30
time (min)
xg=0.0
xg=0.25
Solid: RTF01
Dashed: Tint

Figure 11

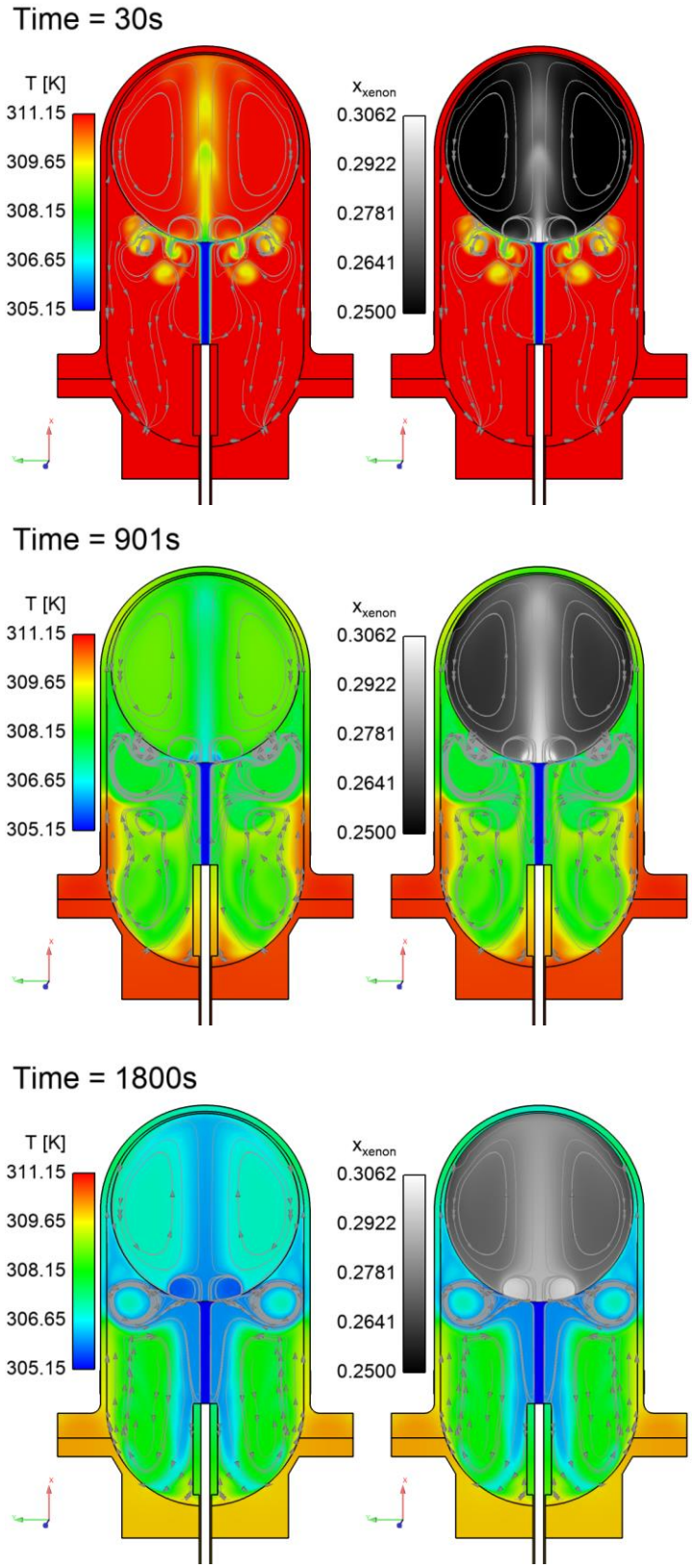
Time = 30s
T [K]
311.15
309.65
308.15
306.65
305.15
x_{xenon}
0.3062
0.2922
0.2781
0.2641
0.2500
Time = 901s
T [K]
311.15
309.65
308.15
306.65
305.15
x_{xenon}
0.3062
0.2922
0.2781
0.2641
0.2500
Time = 1800s
T [K]
311.15
309.65
308.15
306.65
305.15
x_{xenon}
0.3062
0.2922
0.2781
0.2641
0.2500

Figure 12

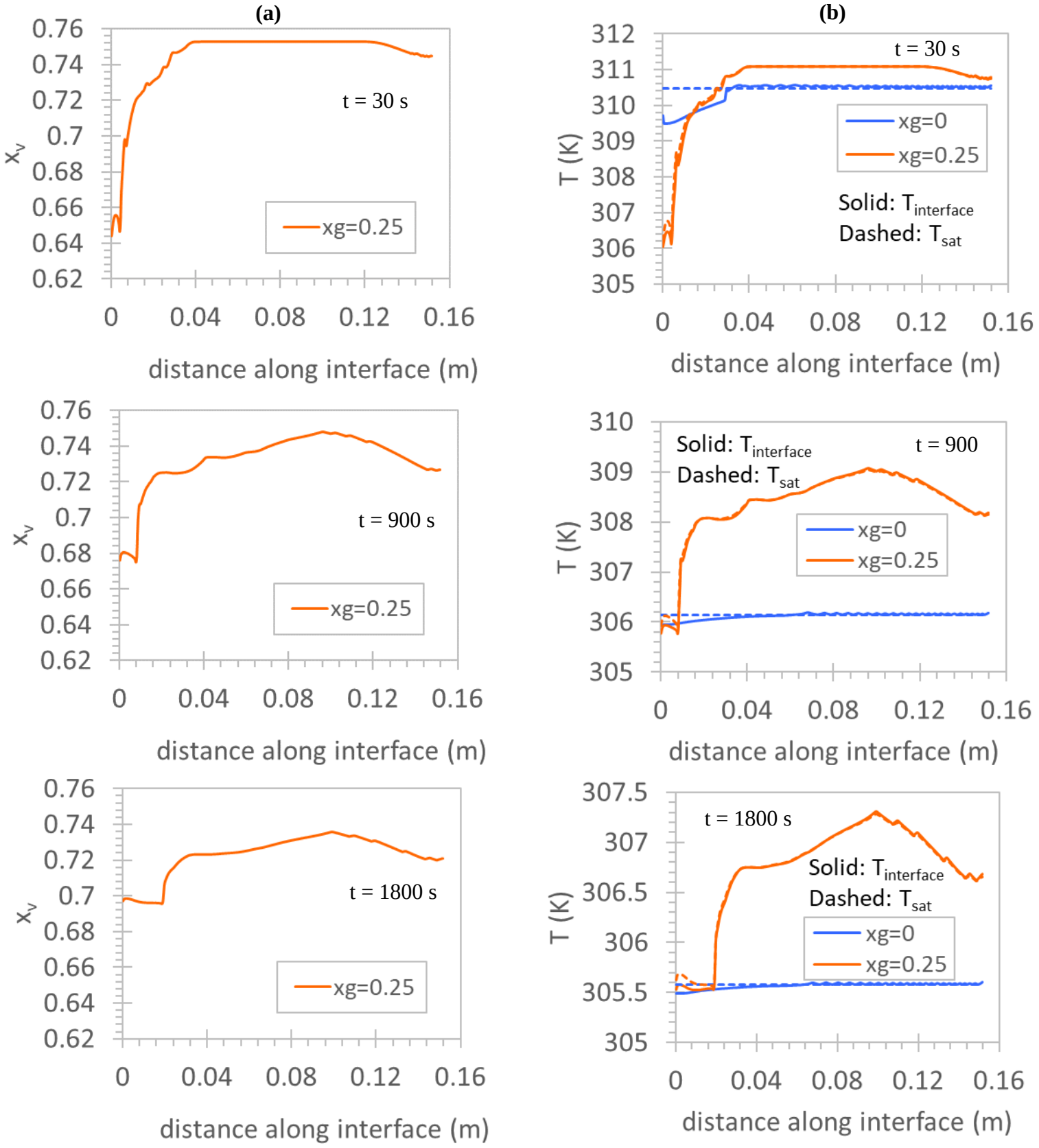
(a)
(b)
t = 30 s
xg=0.25
xg=0
Solid: T_interface
Dashed: T_sat
x_v
T (K)
distance along interface (m)
t = 900 s
t = 1800 s

Figure 13

(c)

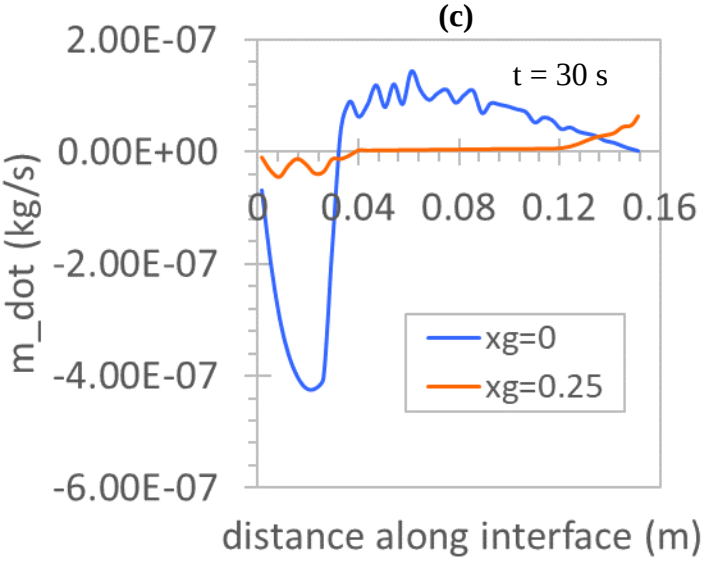

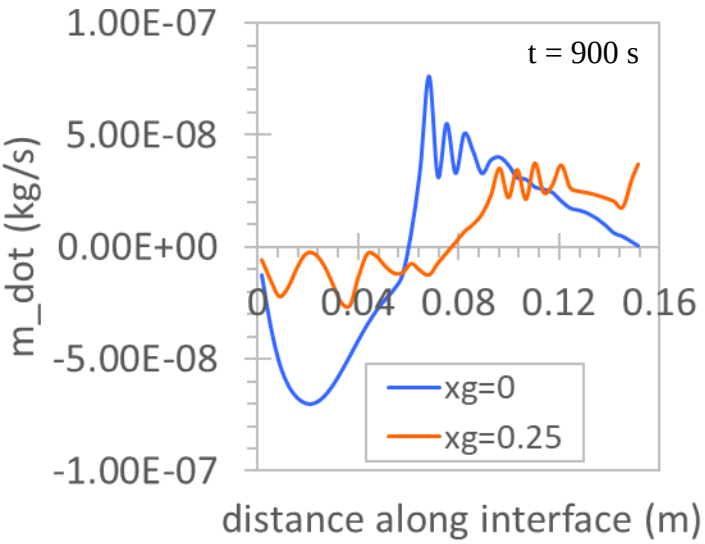

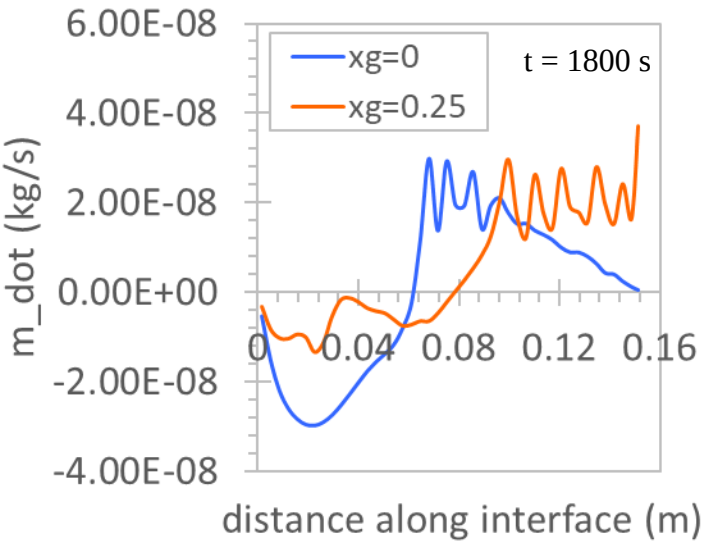

Figure 13 (continued)

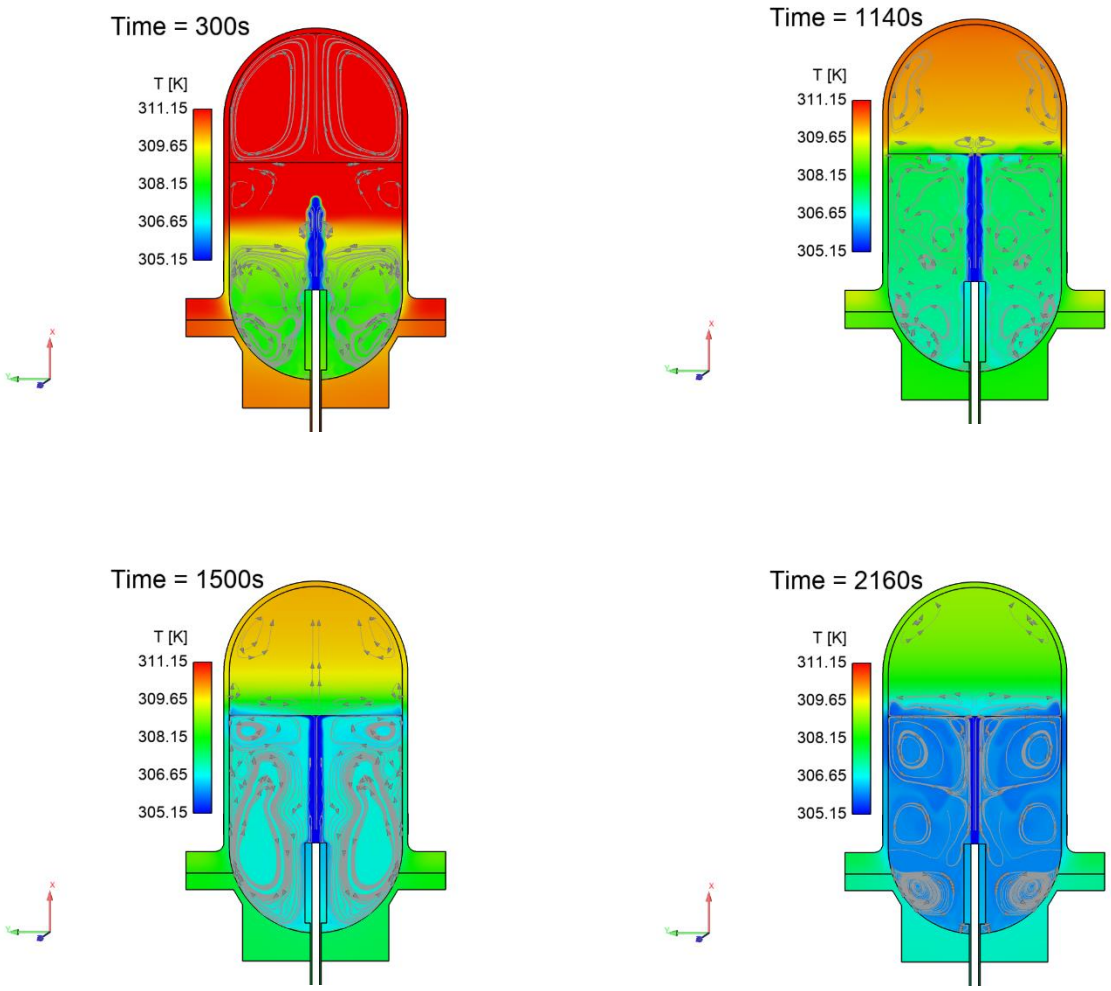
Time = 300s
T [K]
311.15
309.65
308.15
306.65
305.15
Time = 1140s
T [K]
311.15
309.65
308.15
306.65
305.15
Time = 1500s
T [K]
311.15
309.65
308.15
306.65
305.15
Time = 2160s
T [K]
311.15
309.65
308.15
306.65
305.15

Figure 14

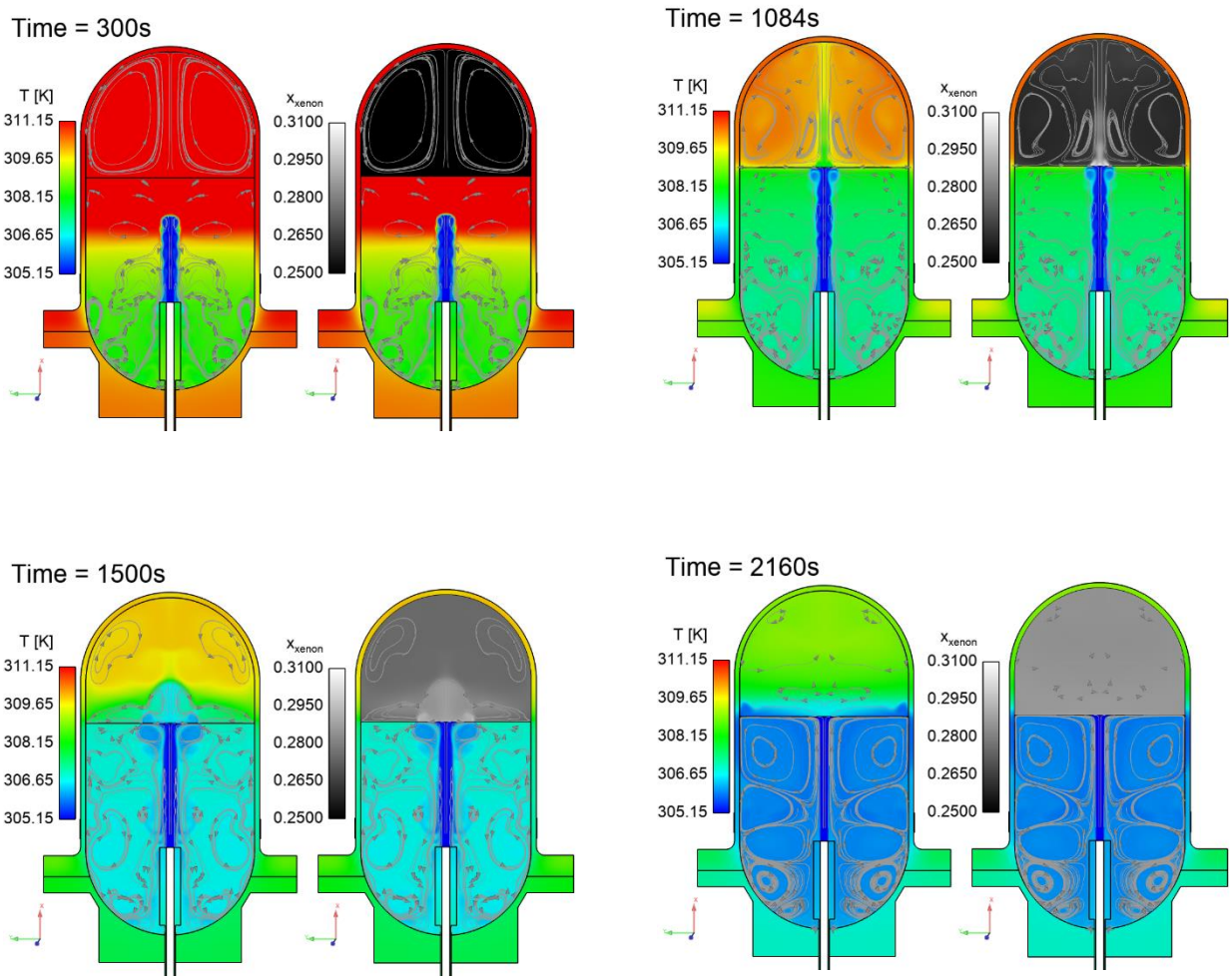
Time = 300s
T [K]
311.15
309.65
308.15
306.65
305.15
x_{xenon}
0.3100
0.2950
0.2800
0.2650
0.2500
Time = 1084s
T [K]
311.15
309.65
308.15
306.65
305.15
x_{xenon}
0.3100
0.2950
0.2800
0.2650
0.2500
Time = 1500s
T [K]
311.15
309.65
308.15
306.65
305.15
x_{xenon}
0.3100
0.2950
0.2800
0.2650
0.2500
Time = 2160s
T [K]
311.15
309.65
308.15
306.65
305.15
x_{xenon}
0.3100
0.2950
0.2800
0.2650
0.2500

Figure 15

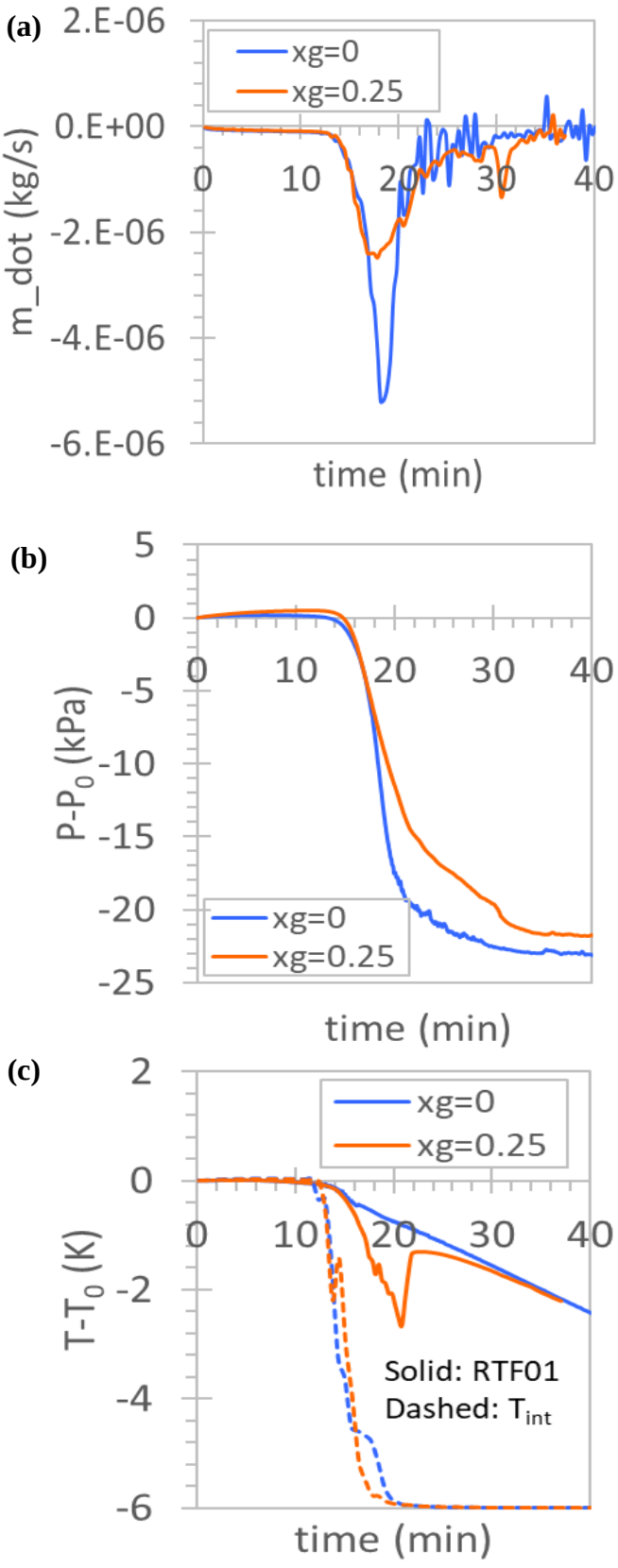
(a)
2.E-06
0.E+00
-2.E-06
-4.E-06
-6.E-06
m_dot (kg/s)
xg=0
xg=0.25
0
10
20
30
40
time (min)
(b)
5
0
-5
-10
-15
-20
-25
P-P0 (kPa)
xg=0
xg=0.25
time (min)
(c)
2
0
-2
-4
-6
T-T0 (K)
xg=0
xg=0.25
Solid: RTF01
Dashed: Tint
time (min)

Figure 16

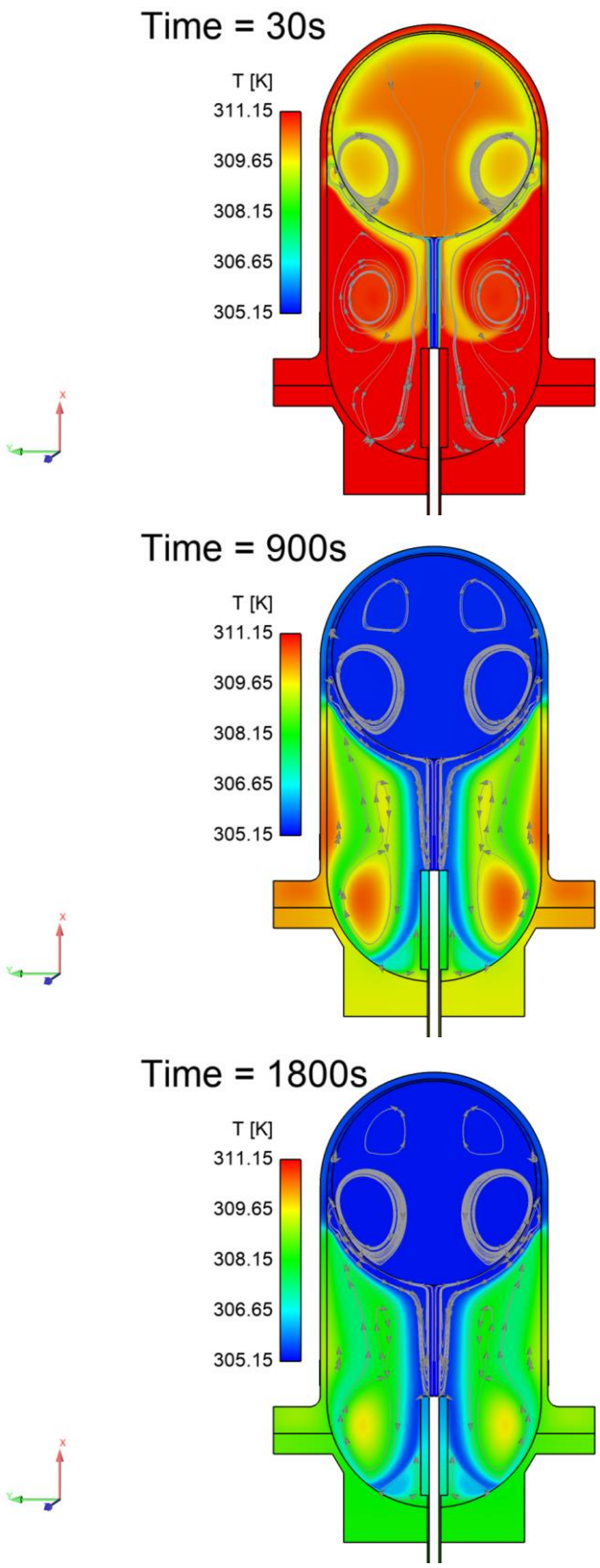
Time = 30s
T [K]
311.15
309.65
308.15
306.65
305.15
Time = 900s
T [K]
311.15
309.65
308.15
306.65
305.15
Time = 1800s
T [K]
311.15
309.65
308.15
306.65
305.15

Figure 17

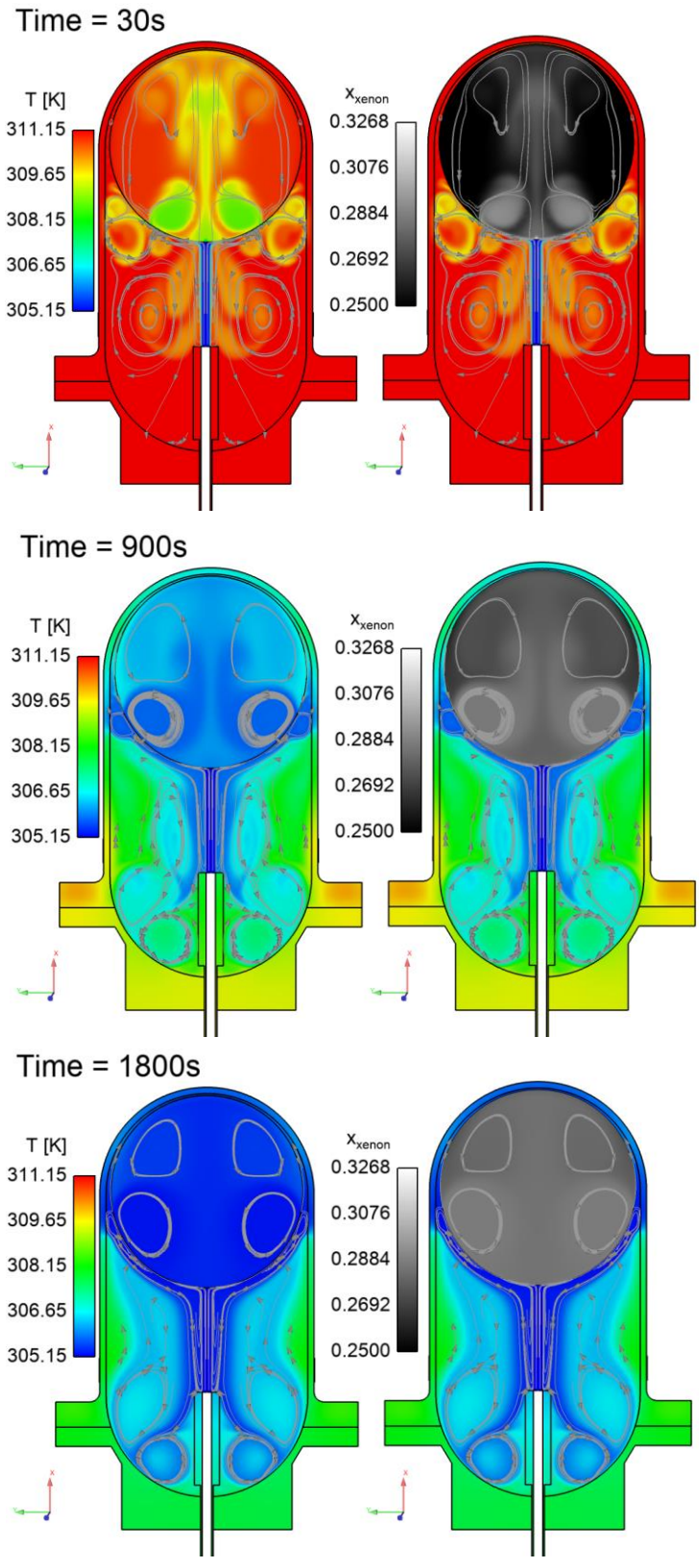
Time = 30s
T [K]
311.15
309.65
308.15
306.65
305.15
x_{xenon}
0.3268
0.3076
0.2884
0.2692
0.2500
Time = 900s
T [K]
311.15
309.65
308.15
306.65
305.15
x_{xenon}
0.3268
0.3076
0.2884
0.2692
0.2500
Time = 1800s
T [K]
311.15
309.65
308.15
306.65
305.15
x_{xenon}
0.3268
0.3076
0.2884
0.2692
0.2500

Figure 18

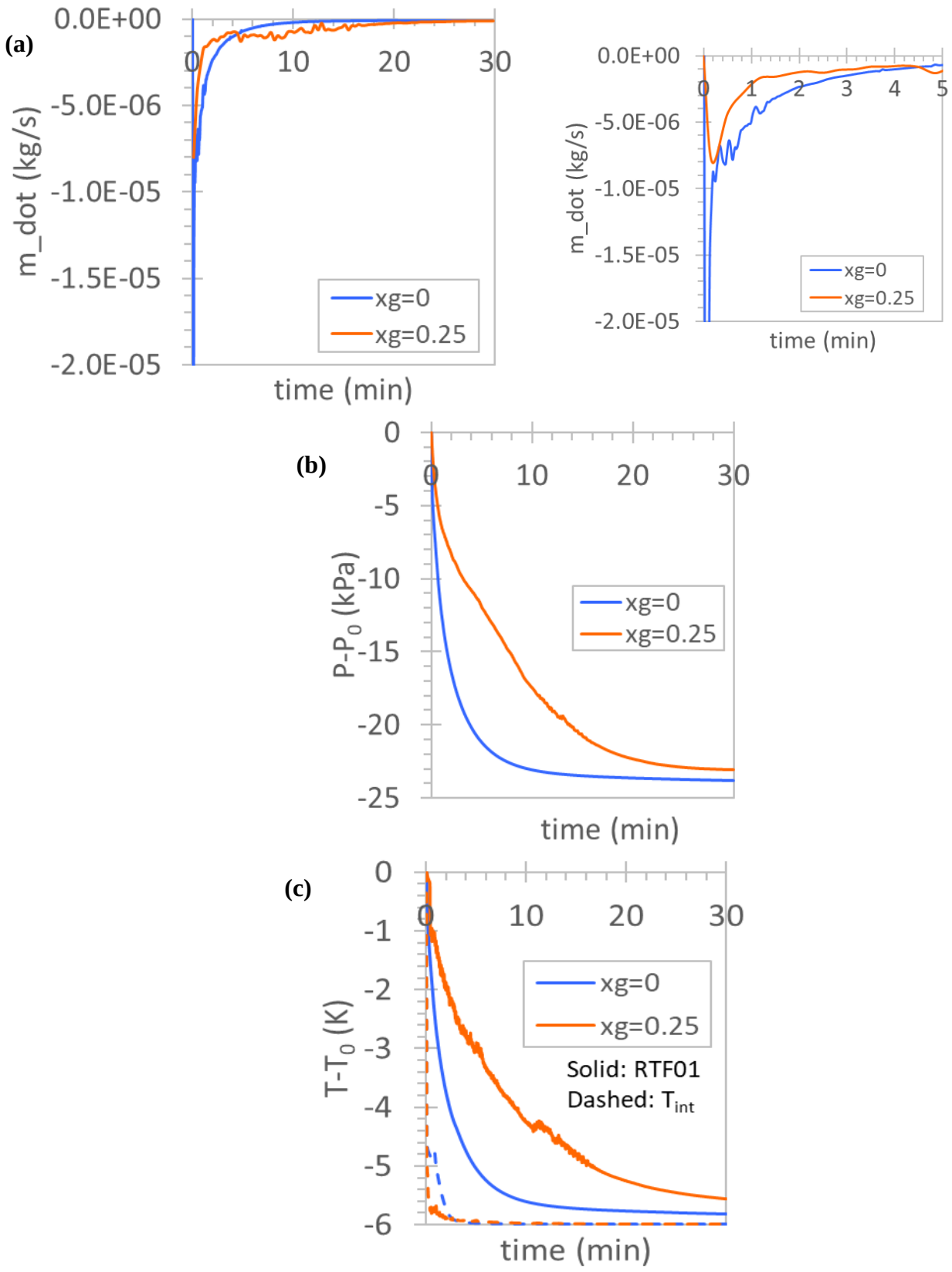
(a)
0.0E+00
-5.0E-06
-1.0E-05
-1.5E-05
-2.0E-05
m_dot (kg/s)
0
10
20
30
time (min)
xg=0
xg=0.25
0.0E+00
-5.0E-06
-1.0E-05
-1.5E-05
-2.0E-05
m_dot (kg/s)
0
1
2
3
4
5
time (min)
xg=0
xg=0.25
(b)
0
-5
-10
-15
-20
-25
P-P0 (kPa)
0
10
20
30
time (min)
xg=0
xg=0.25
(c)
0
-1
-2
-3
-4
-5
-6
T-T0 (K)
0
10
20
30
time (min)
xg=0
xg=0.25
Solid: RTF01
Dashed: Tint

Figure 19